ABSTRACT

Title of Dissertation:	EFFECTS OF EXTERNAL PRESSURE ON SOLID STATE DIFFUSION OF LITHIUM IN LITHIUM-ION BATTERIES
	Nicholas D. Williard, Doctor of Philosophy, 2016
Dissertation directed by:	Professor, Michael Pecht, Mechanical Engineering

Electrochemical-mechanical effects in lithium-ion batteries refer to the phenomena that give way to the piezo-electrochemical properties observed during intercalation of lithium into lithium-ion battery electrodes. By applying perturbations to the external pressure of a lithium-ion battery, the dynamics of lithium intercalation, in particular the diffusion rate of lithium-ions onto and out of battery electrodes, can be studied with respect to the open-circuit potential and the applied hydrostatic pressure. In this study, commercial thin film batteries were subjected to tests in a low-pressure chamber and in a dynamic materials analyzer simulating hydrostatic pressures between 0 and 115 KPa. Under each hydrostatic pressure condition, galvanostatic intermittent titration technique (GITT) was performed to measure and correlate lithium diffusivity to battery strain, open-circuit potential, and applied hydrostatic force. From the data a model was developed for lithium diffusivity as a function of open circuit potential and hydrostatic pressure. The implications of this work extend

from the use of lithiated graphite for energy harvesting and actuation to policy and regulations for how batteries should be safely transported. To provide some insight into how this work can be applied to policy actions, current international regulations regarding the air transport of lithium-ion batteries are critically reviewed. The pre-shipping tests are outlined and evaluated to assess their ability to fully mitigate risks during battery transport. In particular, the guidelines for shipping second-use batteries are considered. Because the electrochemical state of previously used batteries is inherently different from that of new batteries, additional considerations must be made to evaluate these types of cells. Additional tests are suggested that evaluate the risks of second-use batteries, which may or may not contain incipient faults. Finally, this work is extended to supercapacitors through the development of a model to predict the oxidation of functional groups on the surface of graphite electrodes with respect to operational temperature and voltage. This model is used to predict the operational life of supercapacitors and validates the model on accelerated testing data. The final results are compared to previous models proposed in literature.

EFFECTS OF EXTERNAL PRESSURE ON SOLID STATE DIFFUSION OF LITHIUM IN LITHIUM-ION BATTERIES

by

Nicholas D. Williard

Dissertation submitted to the Faculty of the Graduate School of the
University of Maryland, College Park, in partial fulfillment
of the requirements for the degree of
Doctor of Philosophy
2016

Advisory Committee:
Professor Michael Pecht, Chair
Professor Abhijit Dasgupta
Professor Peter Sandborn
Professor Eric Wachman
Professor Chunsheng Wang

Acknowledgements

I would like to thank PCTEST Engineering Laboratory, Inc , the Center for Advanced Life Cycle Engineering (CALCE) at the University of Maryland and the more than 100 companies and organizations that support its research annually.

Table of Content

Chapter 1 Introduction to Electrochemical-Mechanical Coupling

Lithium-ion batteries use lithium-intercalation compounds as electrode materials. These electrodes store lithium within interstitial sites of their lattice structure during charging and discharging as part of the charge transfer process. As a result of the additional mass of lithium stored inside the electrodes, volumetric expansion occurs, notably in the case of graphite, which is used as an anode in most commercial lithium-ion batteries. [1,2] These volumetric changes insinuate a coupling between the electrochemical and mechanical properties of lithium-intercalation compounds. Efforts to model electrochemical-mechanical (EM) effects such as lithium diffusion induced electrode stress have been proposed.[3-13] However, these studies treated lithium intercalation as the preceding cause of electrode dimension change rather than as a mutually coupled EM phenomena. The reverse effect of EM coupling considers how an applied external mechanical force can drive changes in the electrochemical state of the battery that are observable in the measured potential. The implications of such coupling extend the practical applications of a lithium-ion battery system beyond charge storage to actuation, sensing, and energy harvesting.[14]

Studies have been performed to demonstrate that external mechanical force can produce reversible changes in open-circuit potential.[14-17] Hirai et al. [15] showed that elastic-strain energy could influence a Li-Sn electrode potential due to its contribution to Gibbs free energy formation. Ichitsubo et al.[16] investigated strain-induced potential changes during different lithiation phases of a Li-Sn system.

Jacques et al.[14] measured the direct response between open-circuit potential and applied tensile force on lithium-intercalated carbon fibers. They also measured a current response to an applied tensile force while keeping the cell under potentiostatic conditions, thereby proving that external mechanical force can be a driver of lithium intercalation. Jacques et al. [17] later used the EM coupling to construct a working energy-harvesting device out of lithium-intercalated carbon fibers to convert mechanical energy to stored electrochemical energy.

The effect of external pressure on lithium dynamics is driven by the structural reordering of the electrode lattice during phase change. Lithium intercalation electrodes exhibit phase transitions as lithium is inserted into the material at different stages of charge. The application of external pressures changes the phase stability of the electrode materials as demonstrated by Clark et al. [18] and Miyazaki et al. [19], who showed that stage transitions in graphite can be induced isothermally by pressure alone. When an electrode undergoes a phase change, defect concentrations and mobilies are altered [20], resulting in different diffusivity properties of the electrodes [21]. Therefore, ionic diffusion is indirectly affected by external pressure as a result of the phase stability of the electrodes.

Most experimental studies demonstrating the mechanical influences on the electrochemical state of lithium-ion batteries have been empirically based by monitoring the voltage response to applied strain, but give few insights into the internal dynamics of battery operation. [14-17] Theoretical studies attempting to

model full cell EM interactions have assumed a constant diffusion rate rather than accounting for changes in lithium-ion diffusivity as a function of open-circuit potential or applied external force. [10,12,22] While the EM phenomena have been experimentally demonstrated, the underlying physical effects of external mechanical force on lithium-ion dynamics are largely unknown.

This study experimentally demonstrates EM effects on lithium diffusion by measuring the interactions between open-circuit potential, strain, diffusivity, and applied hydrostatic pressure. The results provide the first measurements linking lithium-ion dynamics to applied external pressure, providing insight into the physical mechanism responsible for EM coupling effects. The contributions of external pressure on lithium diffusion rate are statistically validated and modeled and the results are analyzed in order to gain insights into the phenomenon governing the experimental results.

Chapter 2: Material and Methods

Commercial lithium-ion cells were used in this study. The cells were designed in a thin pouched format with dimensions 1 × 46 × 50 mm and rated at 180 mAh. Deconstruction analysis revealed that the electrodes were wound in a spiral roll one time in order to achieve a thin dimension, as shown in **Figure 1**. Energy dispersive spectroscopy confirmed the cell was composed of a graphite anode and $LiCoO_2$ cathode with copper and aluminum current collectors. Scanning electron microscopy performed on the surface of the electrodes showed that larger particle sizes were

upwards of 10 μm. The soft pouched form factor was selected to expose the electrodes to as much external pressure influences as possible.

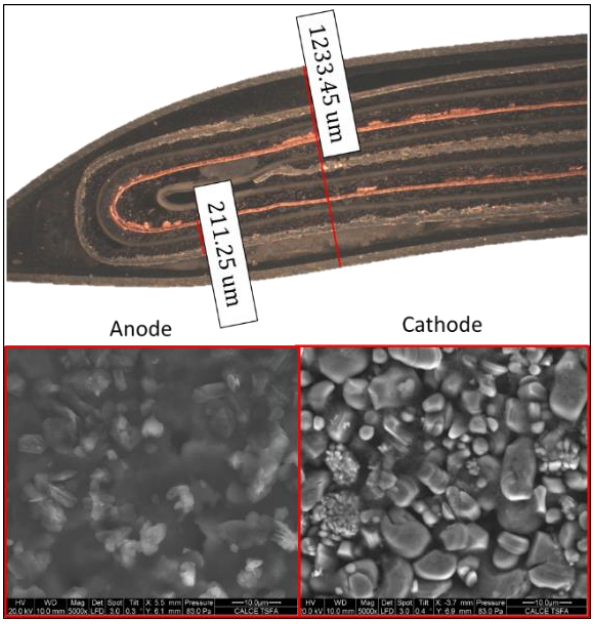

Figure 1 Cross-section of sample used in testing, and ESEM images of electrode surfaces.

Testing was conducted in two phases. For external pressures below standard atmospheric pressure, cells were loaded into a vacuum chamber specified to 0.001 Torr. The chamber was custom ordered (CANATECH Co. Ltd., South Korea) and built to support airtight electrical connections between cells stored in the chamber and an outside battery tester. For external pressures above atmospheric pressure, a hydrostatic condition was simulated in a dynamic materials analyzer (DMA) by placing the cell between two load-distributing surfaces and applying a constant controlled compressive load while measuring the battery's strain response. The thin form factor of the cell allowed the compressive load to be uniformly distributed to

96% of the cell's surface area, only slightly concentrating the load compared to true hydrostatic conditions.

To measure the diffusivity of lithium ions exchanged between electrodes, cells were cycled according to the galvanostatic intermittent titration technique (GITT).[23,24] **Figure 2** shows the discharge voltage profile under GITT. In this experiment, the battery was charged/discharged by alternating current pulses (0.18 A and 0.09 A) each held for 60 s in length and separated by 5 min of rest to allow for the cell to return to steady state after each pulse. The equation shown in **Figure 2** was derived from Fick's second law of diffusion and simplified for short current pulses where lithium does not have a chance to diffuse along the total radial length of an electrode particle. Using this assumption, diffusivity can be measured independent of the length at which lithium has diffused into the bulk electrode, allowing all parameters to be practically measured during testing. This equation assumes a constant electrolyte concentration, which is reasonable for low current pulsing.

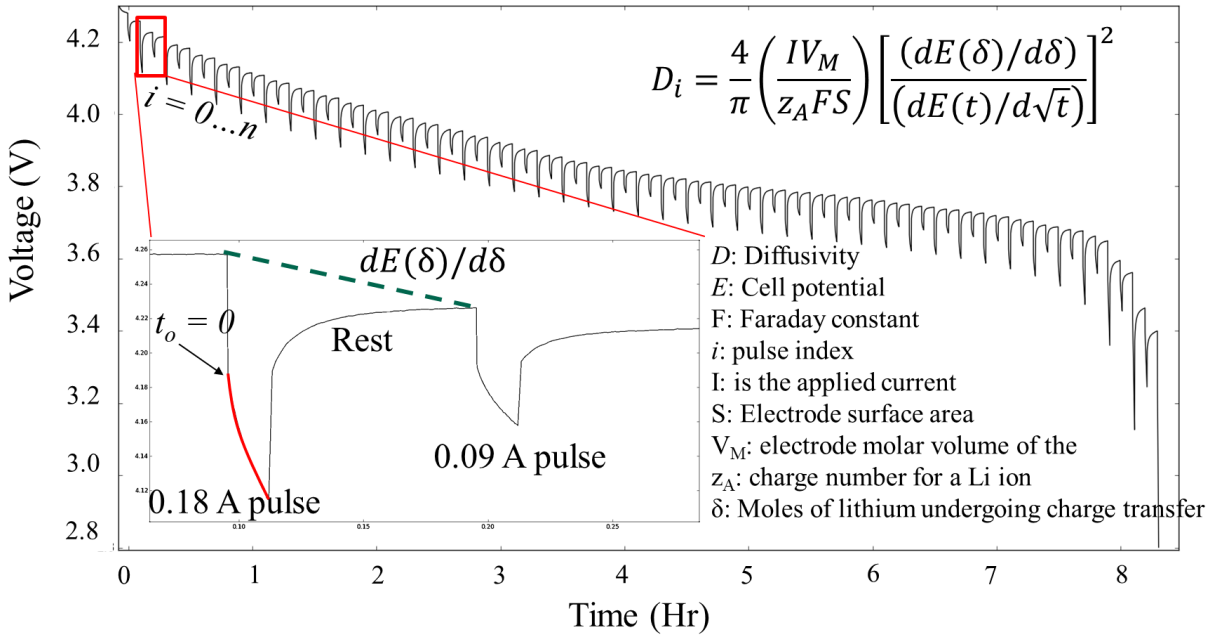

Figure 2 GITT discharge voltage profile, diffusivity model, and parameter names. GITT was applied to the charging profile as well.

Cells were subjected to a range of external pressure conditions and for each condition, two full charge/discharge cycles were performed according to the GITT profile described above. The pressure conditions are summarized in Table 1. Between each pressure test in the vacuum chamber, the GITT was repeated at 100.3 kPa in order to account for any degradation effects that might have occurred due to cycling rather than external pressure influences. Five samples were used in the vacuum chamber and 3 samples underwent testing in the DMA, which provided a total of 2,869 diffusion measurements including both charge and discharge profiles. The maximum pressure achieved during testing was 115.3 kPa. The test was designed to keep external

pressures relatively low so that effects could be observed without damaging the electrodes or applying excessive compression to the separator. The strain response of the cells tested in the DMA was measured and analyzed, however, electrode strain was not measured during low-pressure testing in the vacuum chamber.

Table 1 Experimental test matrix

Ambient Pressure [kPa]	Test	Measurements
100.3[a]	Low-pressure chamber (5 samples)	Voltage, diffusion, ambient pressure
11.6		
6.3		
0.6		
0.01		
102.8	Dynamic materials analyzer (3 samples)	Voltage, diffusion, ambient pressure, strain
105.3		
110.3		
115.3		

[a]Cells were tested at 100.3 kPa after every pressure test to allow for comparison with a reference condition.

Chapter 3: Analysis of Pressure Testing on Lithium-Ion Cells

To ensure that the compressive force used in DMA testing closely represented the hydrostatic conditions used in the low-pressure chamber, Mohr's circle analysis was used to evaluate the shear stress placed on the cells during testing. In the low-pressure chamber, the hydrostatic condition imparts equal normal stress on all sides of the cell, however, in DMA testing a normal force is only applied to the surfaces perpendicular to the load, and, therefore, there is a shear component of stress τ. The stress tensors and Mohr's circle representations are shown in **Figure 3**. In the DMA testing, P_{load} is the compressive load placed on the cells by the tester and P_o is the atmospheric pressure 101,325 Pa. From the non-parametric equation for Mohr's circle, the average normal stress σ_{avg}, the max shear stress τ_{max}, and the percent contribution of shear to total stress $\sigma_{\%}$ can be calculated by:

$$\sigma_{avg} = \frac{1}{2}(\sigma_x + \sigma_y) \quad (1)$$

$$\tau_{max} = \sqrt{\left[\frac{1}{2}(\sigma_x - \sigma_y)\right]^2} \quad (2)$$

$$\sigma_{\%} = \frac{\tau_{max}}{\sigma_{avg} + \tau_{max}}(100) \quad (3)$$

Considering the pressures tested in the DMA, as shown in Table 1, the percent contribution of shear stress $\sigma_{\%}$ on the electrode made up 0.71%, 1.88%, 4.06%, and 6.06% for 102.8 kPa, 105.3 kPa, 110.3 kPa, and 115.3 kPa, respectively. While shear and normal stresses could potentially have a different impact on diffusivity, the

effects of shear stresses used in this testing were considered negligible as they were only a small percentage of the total stress acting on the cells.

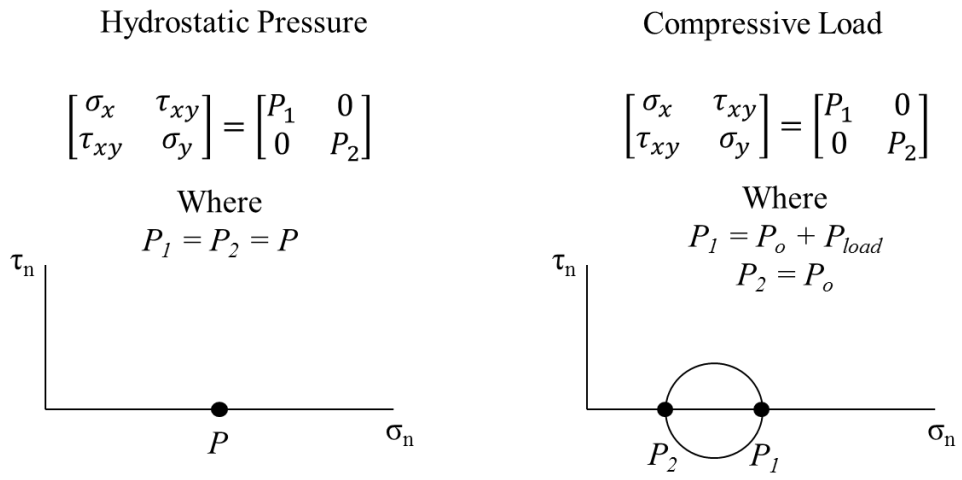

Figure 3 Stress tensors and Mohr's circle representation for the two loading conditions used during testing.

A python script was written to parse the current and voltage data so that individual charge/discharge cycles and current pulses could be indexed and referenced. Indexing enabled the automated extraction of all the features required to calculate diffusion for each current pulse. The resulting diffusivity value produced by GITT is considered an apparent diffusivity and is dominated by the electrode region where diffusivity is limited. In reality, the anode and cathode each have separate diffusivity properties, and within each electrode, the existence of two phase regions can result in different diffusivity properties between localized areas of the bulk electrode. During charging, lithium ions migrate to the anode, and GITT measurements primarily represent the diffusivity of graphite, thus, this is considered the anodic diffusivity profile. During

discharge, lithium ions migrate to the cathode and GITT measurements represent diffusivity in $LiCoO_2$, therefore, this is considered the cathodic diffusivity profile. **Figure 3** shows the resulting diffusivity measurements made during all pressure conditions for both charging and discharging. There was no overlap in the diffusivity measurements between charging and discharge, therefore, the apparent diffusivity value given by GITT can confidently be attributed to each respective electrode.

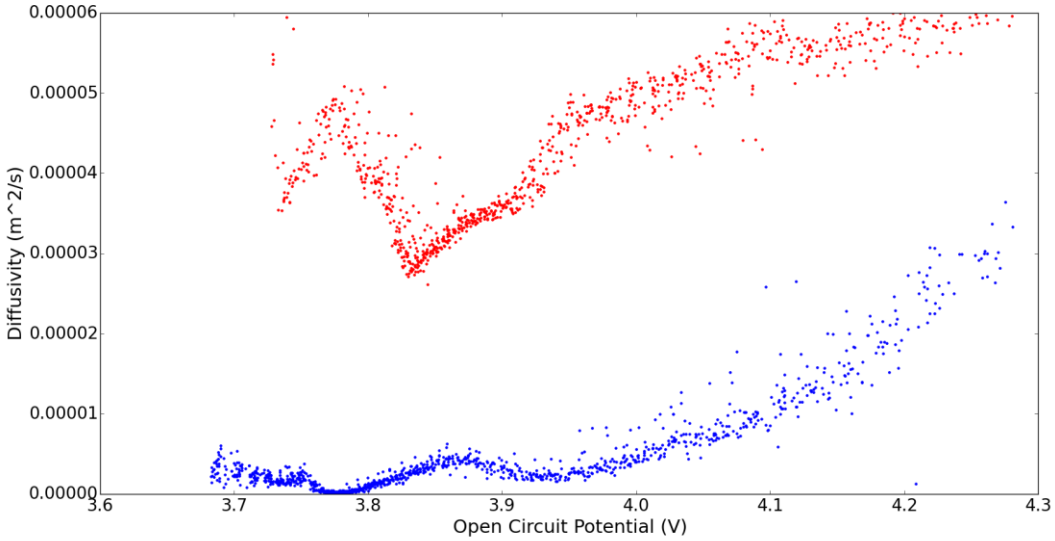

Figure 3 Diffusivity measured during charging and discharging.

The peaks and valleys observed in the diffusivity profile are a result of phase changes in the electrode materials. Phase transitions propagate though the electrode structure in a wave-like front resulting in sweeping transformations across the bulk electrode. [25] During a phase transition, two phase regions exist in the bulk electrode and the diffusivity value produced by GITT represents the combined effect of diffusion in both regions. As the new phase becomes more prominent in the bulk electrode, the diffusivity profile will produce a peak indicating the electrode is in a pure single

stage. In Li_xCoO_2, an order/disorder phase transition from hexagonal to monoclinic occurs around $x = 0.5$ [26], which corresponds to the peak in the discharge diffusivity profile at 3.87 V. During lithium intercalation into graphite, lithium ions must overcome attractive van der Waals bonds between interlayers of carbon. Stage transitions in graphite intercalation compounds refer to the number of graphene sheets between layers of intercalant. During lithium intercalation, graphite stage transformations progress from stage-4 (three non-occupied graphene sheets between lithium intercalation layers) through stage-3, to stage-2 liquid phase where ions assume no in-plane ordering, and finally to stage-1 where every layer is occupied and the battery is in its highest charge state. [27,28] These transitions can be seen in the peaks of the charging diffusivity profile at 3.78 V, 3.88 V, 3.95 V, and 4.1 V, respectively.

The diffusion coefficients calculated for all cells during charging and discharging, and the strain profile measured in the DMA are plotted with respect to open-circuit potential in **Figure 4**. The strain profile shown in **Figure 4** is similar to the strain response of all the cells measured. The strain rate with respect to open-circuit potential is non-constant and correlates to changes in the diffusivity rate. This behavior is expected because a changing flux of lithium ions between electrodes causes the electrode volume to contract at different rates.

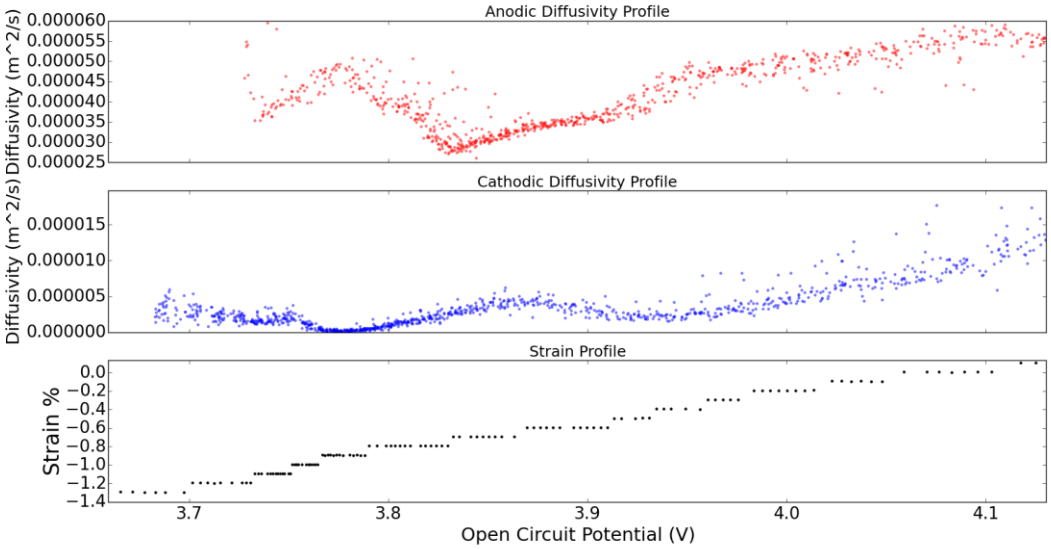

Figure 4 Anodic diffusivity, cathodic diffusivity, and strain profiles plotted with respect to open-circuit potential.

Figure 5 shows the anodic and cathodic diffusivity profiles against open-circuit potential for three of the pressure conditions applied inside of the vacuum chamber, and **Figure 6** shows the diffusivity profiles zoomed in closer to the lower states of charge for four different pressure conditions. An exponentially weighted moving average (EWMA) was applied to each of the individual conditions so that the trend in diffusivity could be easily observed. It was found that the measured diffusivity is the largest at higher states of charge and decreases as the battery is discharged.

The increase of external pressure during charge was shown to facilitate faster ion diffusion at higher states of charge, but at around 3.87 V and below, increased pressure was shown to inhibit ion diffusion. During discharge, the effects were reversed as increased pressure resulted in decreased diffusivity at higher states of

charge and increased diffusivity at lower states of charge. These results were consistent across all external pressures tested, however, only three pressures were shown in **Figure 5** and four pressures in **Figure 6** in order to prevent clutter. All of the pressure data is shown in **Figure 8** after the data was transformed into an ion mobility value.

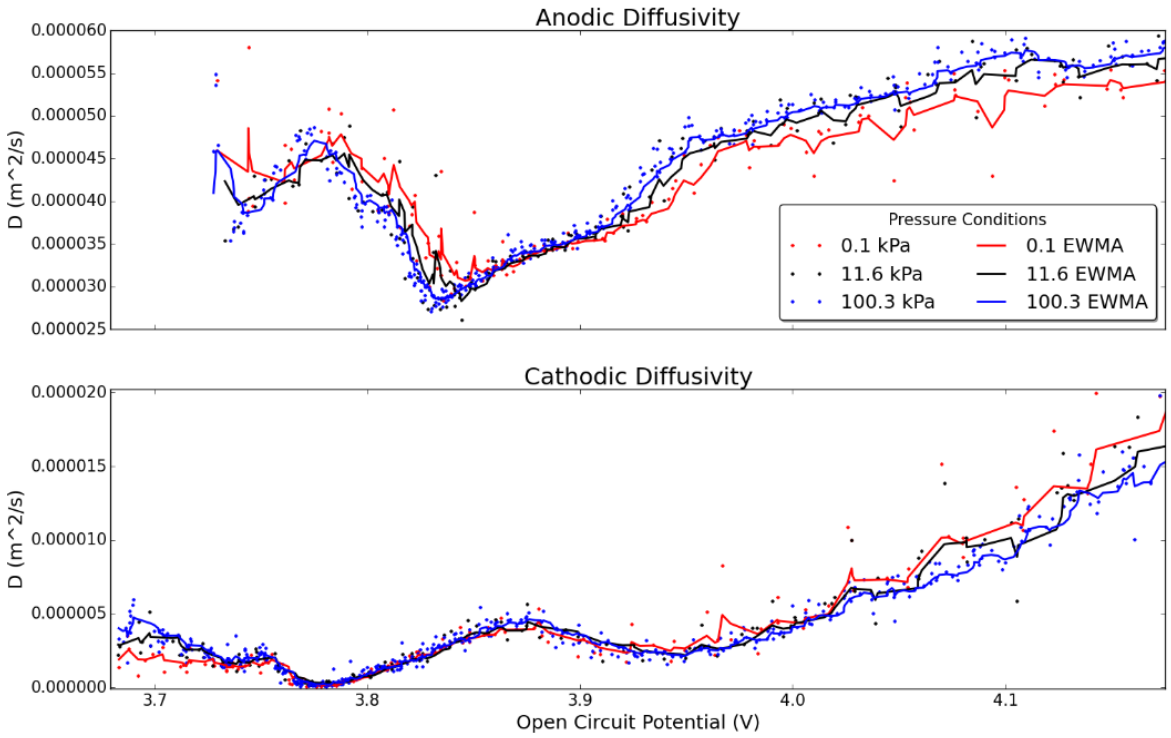

Figure 5 Anodic and cathodic lithium diffusion shown at 3 different external pressure conditions fitted with a EWMA.

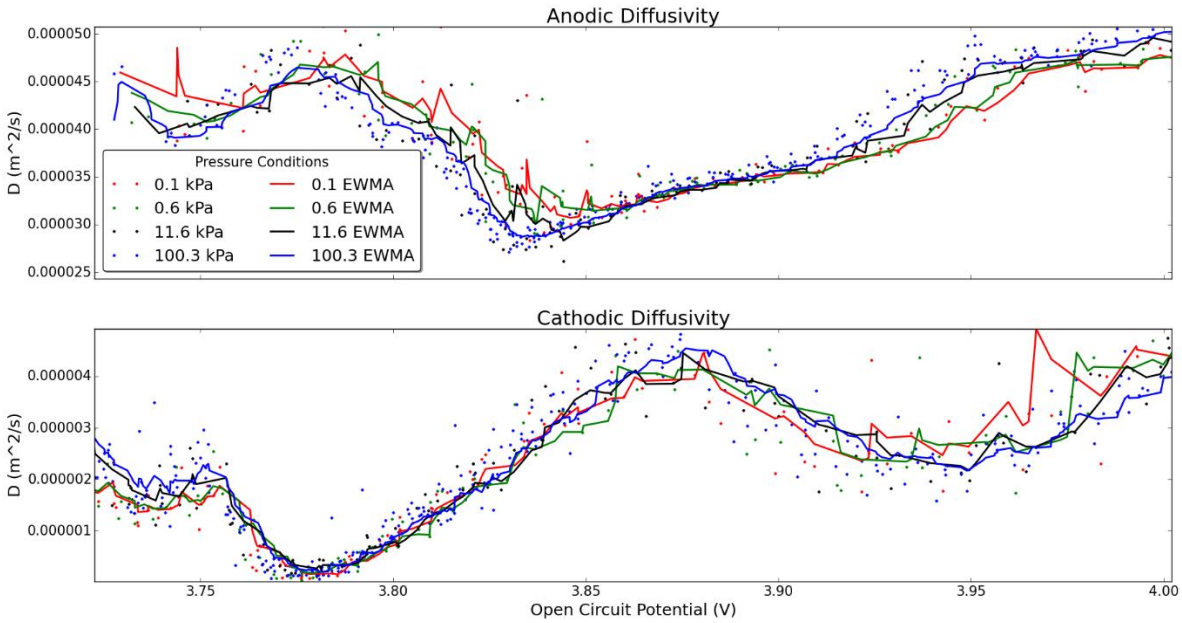

Figure 6 Anodic and cathodic lithium diffusion shown at 4 different external pressure conditions fitted with a EWMA.

The diffusivity data was repeatable but noisy and the EWMA was used to examine the trends in diffusivity with respect to open-circuit potential and applied external pressure. This statistical approach assumes that for each of the individual pressure conditions, the measurement of diffusivity will be drawn from an associated distribution, thereby allowing statistically valid observations based on how the EWMA changes with open-circuit potential and external pressure. In order to validate that the data points sampled from each pressure condition were indeed sampled from separate distributions, a Kruskal–Wallis one-way analysis of variance test was performed. [29]

For this test, the data points were limited to those above 3.92 V to prevent stage transitions from influencing diffusivity measurements. To correct for voltage biases, a smoothed 4th-order polynomial was fit to the data, and the distance of each data point to the smoothed mean was calculated as shown in **Figure 7**. The approximate diffusivity distributions for each pressure can be shown by plotting the histogram of distance measurements for each pressure condition. In **Figure 7**, diffusivity distributions are shown for 100.3 kPa and 0.01 kPa. While there is significant overlap in the two distributions, there is an obvious shift in mean, which can be associated with pressure influences. A Kruskal–Wallis test between the 100.3 kPa and 0.01 kPa data gave a P-value of 1.137E-6, suggesting that the null hypothesis, that the 2 sets of data are drawn from the same distribution, should be rejected (this is based on the historical perspective that a P-value < 0.05 should result in the rejection of the null hypothesis). Furthermore, performing the Kruskal–Wallis test using all of the pressure conditions between 0–115.3 kPa resulted in a P-value of 6.96E-13. This result highly suggests that multiple distributions, each associated with a different pressure, exist in the data.

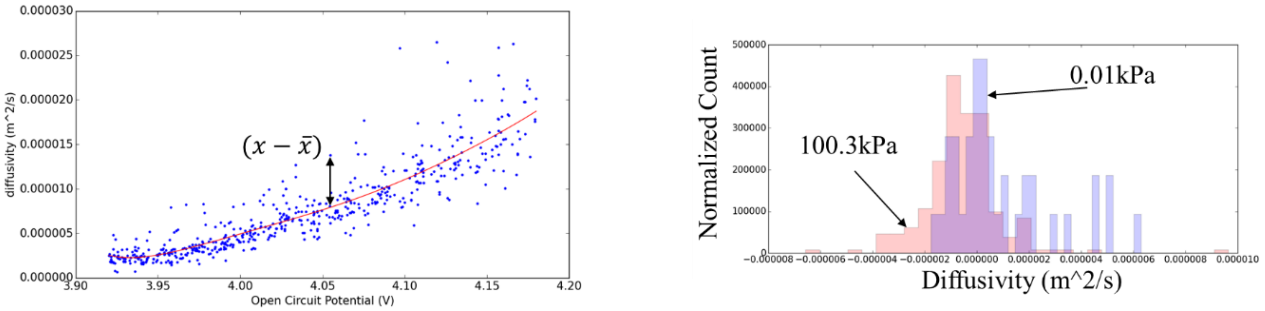

Figure 7 Polynomial fit to diffusivity data above 3.92 V, histograms of diffusivity points at different pressures.

The behavior of external pressure on lithium diffusivity in a battery can be attributed to how external pressure is influencing both the anode and the cathode materials. When the external pressure on a battery is increased, the diffusion in each electrode will be affected differently. In the electrode that is donating lithium ions (during discharge, this is the anode) an increased pressure facilitates diffusion out of the anode by accelerating the movement of the phase boundary. However, the electrode that is accepting lithium ions is inversely affected by the applied pressure, making it harder for lithium ions to diffuse into the bulk electrode. Considering this, it is interesting how the increase in external pressure affects the diffusivity differently depending on the state of charge. This would suggest that the net effect of pressure on both electrode diffusivities shifts to be dominated by each electrode over the course of a charge or discharge.

3.1 Pressure-Diffusivity-Open Circuit Potential Model

In order to model the behavior of diffusivity under different pressure conditions, the ion mobility was considered. Ion mobility has been proven to be directly related to ion diffusion by the Einstein relation. [30]

$$D = \mu k_B T \tag{4}$$

where μ is ion mobility, k_B is Boltzmann's constant, and T is temperature in Kelvin. The influence of pressure on ion mobility is a topic of considerable research in ion

mobility spectrometry, where calibrations based on external temperature and pressure conditions are required. [31] Generally, ion mobility is expressed in terms of a reduced ion mobility value, which gives the adjusted value of ion mobility based on the pressure and temperature. By extending this idea to electrochemical systems, the change in lithium-ion mobility can be modeled with respect to a reference ion mobility measurement at a single pressure condition.

The model is derived from the cathodic diffusivity data and can be applied to the charging data by inverting diffusivity with respect to the open-circuit potential. All of the diffusivity measurements were transformed to ion mobility ($m^2V^{-1}s^{-1}$) as shown in **Figure 8**. Values between 3.75 V and 3.92 V were removed to minimize the influence of phase transitions on the ion mobility measurements. The diffusivity measurements taken at 100.3 kPa were selected as the reference ion-mobility values, and they are displayed as blue triangles. A 6-ordered polynomial was fit to the reference data (shown as the blue line in **Figure 8**) so that the distance between the reference values and the data points measured at other pressure values could be calculated. This distance measurement $\mu_o - \mu_{100.3}$ is equivalent to the reduced ion mobility value.

The delta values ($\Delta\mu$) between reduced ion-mobility and $\mu_{100.3}$ are plotted in **Figure 9** and colored according to their respective external pressure conditions. For each pressure condition, a linear fit was applied to the data. The data show that the rate of change in $\Delta\mu$ with respect to open-circuit potential (E) changes with pressure. At

pressures greater than 101.3 kPa, $\Delta\mu$ decreases as state of charge increases and at pressures lower than 101.3 kPa $\Delta\mu$ increases with a higher state of charge. To investigate this behavior, the slope of the fitted reduced ion-mobility curves was plotted with respect to the applied hydrostatic pressure as shown in **Figure 10**.

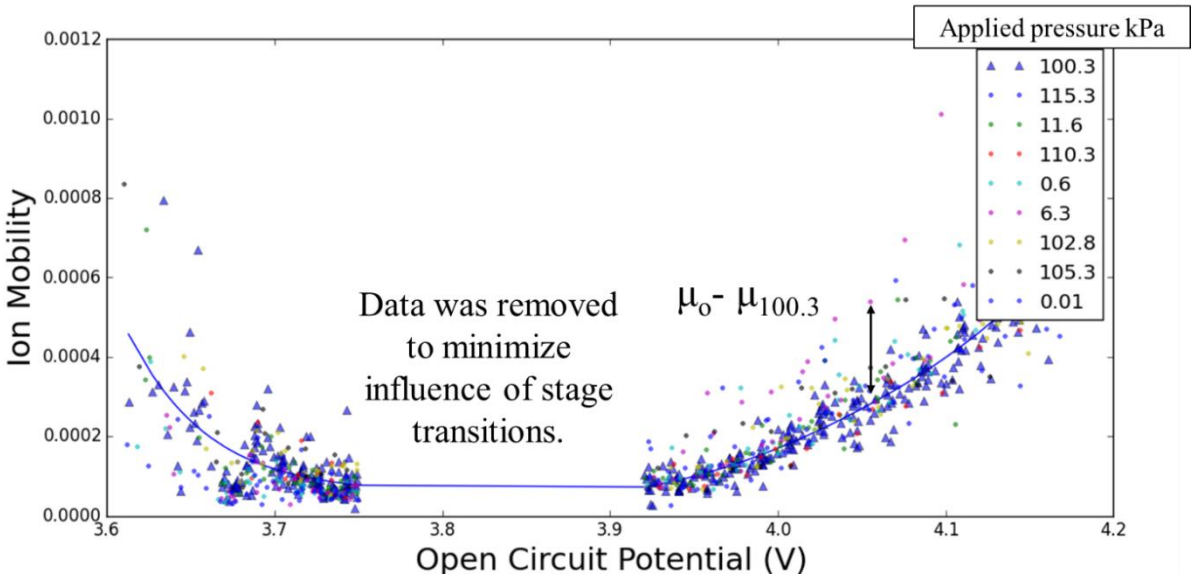

Figure 8 Values of ion mobility plotted vs open-circuit potential. The reduced ion-mobility measurement was observed by subtracting from the average value of ion mobility at 100.3 kPa.

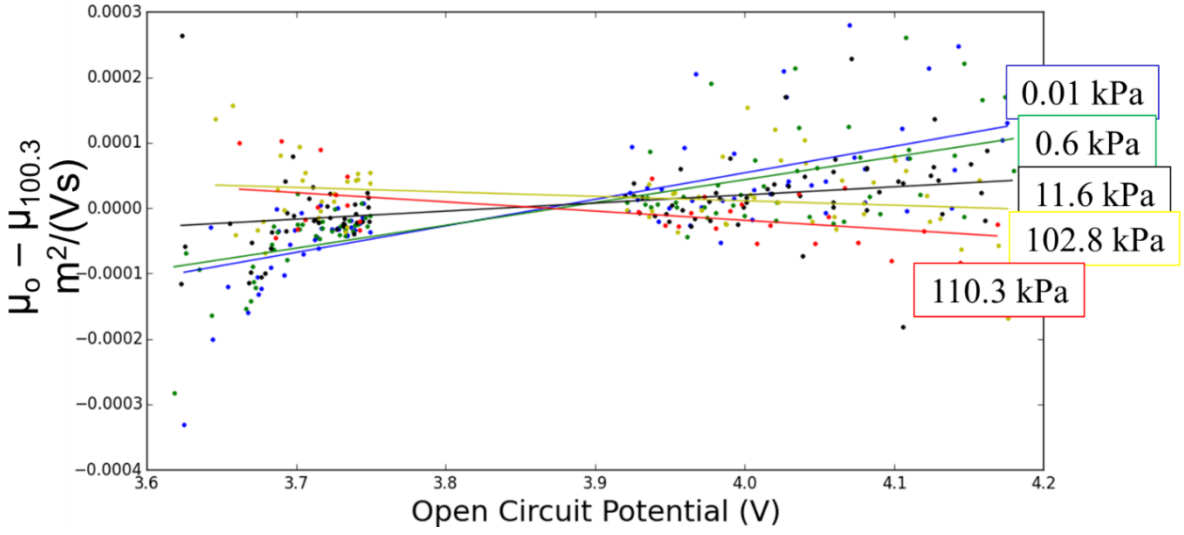

Figure 9 Reduced ion-mobility values shown for each pressure condition.

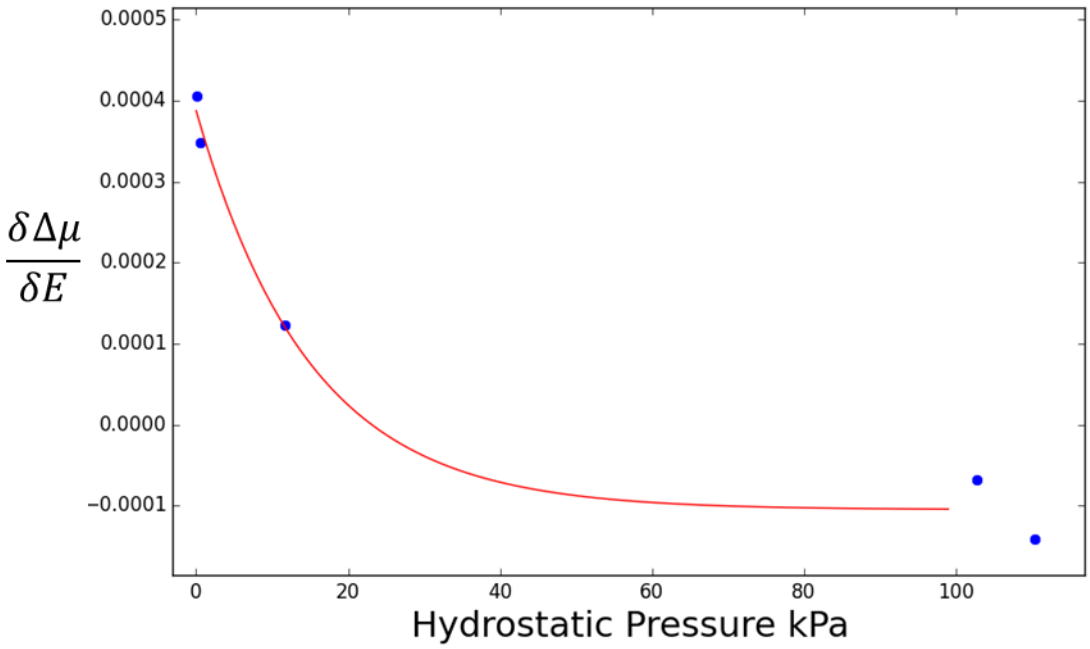

Figure 10 Rate change in $\Delta\mu$with respect to open-circuit potential plotted vs hydrostatic pressure.

Figure 10 shows that the rate change of reduced ion mobility with respect to open-circuit potential decreases exponentially with increased hydrostatic pressure. A decreasing exponential curve was used to fit the data as shown in red. The fit was of the form:

$$\frac{\partial \Delta \mu}{\partial E} = ae^{-bP} + c \qquad (5)$$

where $\frac{\partial \Delta\mu}{\partial E}$ is the rate that the reduced ion-mobility value changes with open-circuit potential, *P* is hydrostatic pressure, and *a*, *b*, and *c* are fitting parameters. The parameter *c* is equal to $\frac{\partial \Delta\mu}{\partial E}$ in the case where $\lim_{P\to\infty} ae^{-bP}$. This means that *c* can be considered a lower limit to $\frac{\partial \Delta\mu}{\partial E}$ while the upper limit of $\frac{\partial \Delta\mu}{\partial E}$ is equal to *a* + *c* and occurs at a hydrostatic pressure of zero. The parameter *b* determines the shape of decay of $\frac{\partial \Delta\mu}{\partial E}$ with increasing pressure. This parameter governs the sensitivity of ion mobility with respect to open-circuit voltage for different pressures. Therefore, the parameter *b* has some physical significance in relating the way external pressure influence phase stability at different voltage levels.

By knowing how $\frac{\partial \Delta\mu}{\partial E}$ changes with respect to pressure, a model can be constructed to estimate the reduced ion mobility as a function of voltage and pressure. **Figure 9** shows that the fitted trends of $\Delta\mu$ intersect at approximately 3.87 V. This intersection point will be considered the nominal voltage E_o, and it roughly indicates the open-circuit potential at which external pressure effects on diffusion become inverted. By simply using the point slope form with the fixed point (E_o, 0) and substituting equation 2 for the slope, $\Delta\mu$ can be described as:

$$\Delta\mu(E,P) = ae^{-bP}(E - E_o) - c(E - E_o) \qquad (6)$$

Zero is used as the $\Delta\mu$ axis fixed point because it is considered the reference point where $\mu_o - \mu_{100.3} = 0$. Using least-squares to fit eq. 6 to the diffusivity data collected during this study resulted in 0.00049, 0.06691, and –0.00010 for parameters *a*, *b*, and *c*, respectively. The model output is shown as a surface in **Figure 11**.

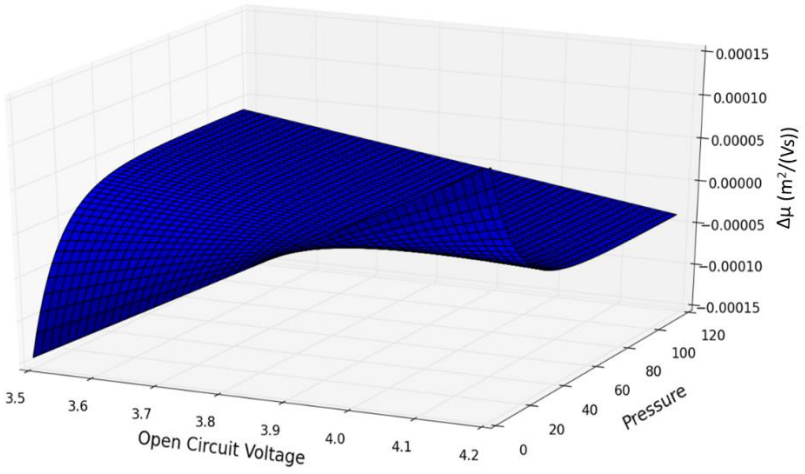

Figure 11 Results of the reduced ion-mobility model fitted to the diffusivity data.

In order to obtain the diffusivity as a function of voltage and pressure, $\Delta\mu + \mu_{100.3}$ can be substituted for μ in equation 3, and the relationship for $\Delta\mu$ in eq. 6 can be inserted to result in:

$$D(E,P) = k_B T[ae^{-bP}(E - E_o) - c(E - E_o) + \mu_{100.3}] \qquad (7)$$

where $\mu_{100.3}$ is a function of E.

The results provide insight into solid-state lithium diffusion and offer a means to evaluate how pressure contributes to the phase stability and resulting diffusivity of each electrode.

When external hydrostatic pressure is added to a battery system, it applies a compressive force on the electrodes. During charging/discharging, an increase in external compressive force increases diffusion in the electrode that is donating ions by accelerating the movement of the phase boundary in the respective electrode. For the electrode that is accepting ions, an external compressive force increases the total interlayer binding energy that must be overcome by a lithium ion in order for charge transfer to occur which hinders diffusion. Throughout discharge, the compressive force is being applied to both electrodes, however, changes in lithium concentration and structural changes induced by staging phenomenon in individual electrodes, change the net effect that external stress has on the perceived lithium diffusion rate.

The diffusivity measurements shown in Figure 5 allow us to specifically evaluate the effect of pressure on each of the electrodes. For the anodic curve, diffusivity was calculated during charging so the $LiCoO_2$ electrode was donating lithium ions and the graphite electrode was receiving ions. For charging, the diffusivity profile proceeds in time from left to right, so towards the beginning of charging at open-circuit potentials below 3.87 V, it can be seen that an increase in pressure reduces ion diffusivity. In this region, diffusivity is influenced more heavily by the net effect of pressure on the anode (graphite) as this is the receiving electrode and the electrode in which a compressive force would result in an inhibiting effect on diffusivity. At

voltages above 3.87 V, an increase in diffusivity is observed with increasing pressure, suggesting that diffusivity is more heavily influenced by the effects of pressure on the $LiCoO_2$ cathode, which would result in an overall facilitation of diffusion within the cell.

The data in the cathodic diffusivity profile suggests that the pressure-diffusivity behavior is reversed during discharge. This is intuitive as the lithium ions are migrating toward the opposite direction and the diffusivity profile proceeds in time from right to left. At voltages above 3.87 V, an increase in pressure results in a decrease in diffusivity, which implies that the pressure effects on the cathode contribute the most towards the diffusivity measurement because in this case, the cathode is the receiving electrode. Similarly, as discharge continues to voltages below 3.87 V, the main contributing electrode towards the influence of pressure on diffusivity switches to the anode and an increase in diffusivity is observed at increasing pressure.

Chapter 4: Summary of External Pressure on Lithium-ion Cells

In this study, lithium diffusivity was measured in cells at different pressure conditions. The influence of pressure and voltage on diffusivity was modeled and fitted to the experimental data. It was found that pressure affects diffusivity differently depending on the state of charge of the cell. Particularly, an increase in pressure inhibits diffusion at the beginning of a charge or discharge profile, but facilitates diffusion toward the end of the profile. This is due to the opposing effects that external pressure has on each of the individual electrodes inside a cell. Diffusion

in the electrode-donating ions is accelerated by external pressure whereas diffusion in the electrode-receiving ions is inhibited. The evolving concentration of lithium within each electrode during a charge or discharge process changes the electrode that dominates the net pressure effect on diffusivity.

This is the first paper to provide a pressure- and voltage-dependent model for diffusivity. The model is semi-empirical, but physical significance is attached to each of the model-fitting parameters. The model predicts the observed behavior of the diffusivity/pressure relationship inverting itself over the course of a discharge.

Chapter 5: Overview of Battery Air Transportation Standards

The shipment of lithium-ion batteries poses serious safety concerns especially during air travel. A short circuit in a single cell is capable of creating enough heat to result in cascading failures of adjacent batteries, leading to a catastrophic incident. While lithium-ion batteries are generally protected by redundant safety features and controlled by a battery management system (BMS) that prevents operation at excessive voltages and temperatures during use, the same protection is not practically implemented during transportation of large quantities of lithium-ion cells. Constant monitoring during use ensures that batteries remain within safe operating limits and warns the user if anomalous behavior occurs. However, batteries shipped as cargo outside of a host device have no active monitoring or control of voltage or temperature. This is problematic when large quantities of cells are shipped.

Safety concerns over the shipment of lithium-ion batteries were highlighted after a United Parcel Service cargo plane carrying a significant number of lithium-metal and lithium-ion batteries crashed in Dubai in September 2010. In July 2013, the United Arab Emirates General Civil Aviation Authority published its final report on the incident and concluded that flaming electrolyte from ruptured lithium cells resulted in the spread and sustainment of the fire [32]. In response to the questionable safety of lithium-ion batteries as cargo, the International Civil Aviation Organization (ICAO), a United Nations special agency, made several updates to their 2013–2014 *Technical Instructions for the Safe Transport of Dangerous Goods by Air* (Doc 9284) regarding the transport of batteries [33]. As large-format lithium-ion batteries were already under strict regulation, the changes in the document mainly addressed smaller battery types of less than 20 Watt-hours (Wh) per cell.

This paper provides a critical review of the current international regulations governing the shipment of lithium-ion batteries by air. The shipment of both new and degraded batteries is considered. With the increased use of lithium-ion batteries across many industries, there is a significant need for transporting degraded batteries for recycling or second-use applications. However, the risks associated with batteries that have prior usage histories have not been thoroughly evaluated and addressed.

Chapter 6: Current Regulations

The regulatory agency responsible for setting guidelines for the transport of lithium and lithium-ion batteries is the International Air Transportation Association (IATA), a trade association comprised of 240 airlines. The IATA's practices regarding

lithium-ion battery transportation have been adopted by many government aviation authorities including the U.S. Federal Aviation Administration (FAA). The documents outlining the provisions for lithium and lithium-ion battery transport are the ICAO's *Technical Instructions for the Safe Transport of Dangerous Goods by Air* [33] and the IATA's *Dangerous Goods Regulations* [34].

Different classifications have been designated for lithium-ion cells and batteries transported individually (listed under UN 3480 in the United Nations regulations for Transportation of Dangerous Goods [33]) as opposed to cells and batteries transported inside a piece of equipment (UN 3481). A lithium-ion cell is defined as a single electrochemical unit consisting of one anode and one cathode inside a single encasing. Lithium-ion batteries consist of multiple cells wired in series or parallel. In some cases, transport regulations for cells and batteries are slightly different. For lithium-ion batteries or cells transported individually, short-circuit protection is required. This means that an electrically isolating material must be placed on the cell terminals to prevent a short circuit. Additionally, when shipping multiple batteries or cells in bulk, each unit must be completely separated by a barrier and then placed in a "strong rigid outer packaging," however, further specifications on the type of packaging that should be used are not provided. The total package must be subjected to and pass a 1.2-m drop test and cannot weigh more than 10 kg. The package must contain documentation, including a shipper's declaration that states "Dangerous Goods as per Attached DGD" or "Dangerous Goods as per Attached Shipper's Declaration." An additional document must be included that states:

"Package contains lithium-ion cells or batteries. Handle with care. When package is damaged can cause fire. Special procedures should be followed: inspect the package and arrange repack by qualified persons when required. Contact Nr: 00XX XXXX XXX XXX."

The final package must include the label shown in Figure 1 with minimum dimensions of 120 mm wide and 110 mm high.

For cells or batteries shipped inside a device, external short-circuit protection is also required. The short-circuit protection of batteries in a device is described in special provision A164 [33] as "disconnection of the battery and protection of exposed terminals." Any additional cells that may be included as spares should be individually wrapped. The device must then be placed in an outer packaging, however, the UN provides no specifications for this packaging. The maximum number of cells or batteries per package is the number of cells required to power the device as well as two spare cells or batteries. The maximum weight of lithium-ion cells or batteries per package must not exceed 5 kg for passenger aircraft but may be up to 35 kg for cargo aircraft for cells greater than 20 Wh and batteries greater than 100 Wh. For documentation, the following statement must be placed on the waybill:

"Lithium Ion Batteries in compliance with Section II of PI966."

An additional document must be included that says:

"Package contains lithium ion cells or batteries. Handle with care. When package is damaged can cause fire. Special procedures should be followed: inspect the package and arrange repack by qualified persons when required. Contact Nr: 00XX XXXX XXX XXX."

Figure 1 Labeling required for packages containing lithium-ion batteries or products with installed lithium-ion batteries to be shipped by air [33]. Reproduced with permission of the United Nations.

Manufacturers must certify that all cells or batteries that are shipped have been manufactured under a quality management program as specified in the Dangerous Goods Regulations (DGR) 3.9.2.6. Additionally, all cells and batteries must be tested in accordance with the UN's *Manual of Tests and Criteria*, Part III, Subsection 38.3 [33] (DGR 3.9.2.6).

Compliance Tests

The UN's *Manual of Tests and Criteria* lays out 8 tests that a rechargeable lithium-ion cell or battery must pass to satisfy regulatory guidelines and be cleared for air

shipment. The first 5 tests must be sequentially performed on a single cell or battery without failure at any point during the tests. If the tests only involve cells, then each test must be repeated for 10 samples in a fully charged state and 10 samples in a fully discharged state. If the tests include batteries, then the tests must be performed on 4 fully charged batteries and 4 fully discharged batteries. Failure is defined as: mass loss (0.5% for cells under 1 g, 0.2% for cells greater than 1 g and less than 75 g, and 0.1% for cells greater than 75 g), electrolyte leakage, venting, rupture, or fire. The 5 tests are described below.

Altitude simulation: The altitude simulation test qualifies a cell or battery under low-pressure conditions such as those that may be experienced on board an aircraft. This test requires the cell or battery to be stored at a pressure of 11.6 kPa or less for at least 6 h without failure. The open-circuit voltage must not decline by more than 10% during the test.

Thermal: A temperature cycling test is implemented to assess the quality of the casing seal and the internal electrical connections. This test is conducted by storing the cell or battery at 75 °C for a minimum of 6 h followed by an additional 6 h of storage at –40 °C with no more than 30 min between the temperature extremes of both tests. This cycle is repeated 10 times.

Vibration: A cell or battery could be subjected to vibration loads during transport, leading to potential safety issues. This test is performed by vibrating the cell using a

sinusoidal waveform with a logarithmic sweep from 7 Hz to 200 Hz and back in a 15-min time period. This is repeated 12 times for three different perpendicular mounting positions with one of the vibration directions perpendicular to the terminal face.

Shock: The shock test assesses the ability of the cell or battery to withstand large mechanical impacts during transport. This test is performed in a drop testing fixture, and the cell or battery should be subjected to a half-sine shock with maximum acceleration of 150 g_n and a pulse duration of 6 ms. The test is repeated 6 times for 3 different mounting conditions for a total of 18 shocks. Each of the 3 mounting conditions should be mutually perpendicular axes.

External short circuit: The external short-circuit test simulates the cell or battery's behavior under exposure of an external short circuit. This test should be performed at a temperature of 55 °C, and the external shorting resistance should be less than 0.1 Ω. This test is sustained for a 1-h period or until the battery casing temperature has returned to a temperature of 55 °C. A battery failure must not occur during the 6-h period following the test.

The remaining 3 tests per the UN's *Manual of Tests and Criteria* can be performed on a new cell or battery as follows:

Impact: The impact test is performed by placing the cell or battery on a flat surface and then placing a 15.8-mm-diameter bar across the center of the cell or battery. A

9.1-kg mass is dropped from a height of 61 cm onto the cell or battery resulting in a kinetic energy of 54.4 J. Each cell or battery must meet the above-mentioned failure criteria, in addition to the requirement that the external temperature does not exceed 170 °C and there is no fire within 6 h after the test is performed. This test must be repeated 5 times with each of the cells or batteries at 50% of its rated state of charge (SOC).

One criticism of the impact test is that it fails to capture the average impact force imparted onto the battery. In order to measure this force, the work–energy principle must be applied by also measuring the kinetic energy of the mass after impact. To do this, the distance traveled by the mass after impact should be measured. The standard should be modified such that the test achieves a constant impact force for all batteries to account for different geometries and materials. Additionally, the test should be performed on batteries at 100% SOC to evaluate the worst-case scenario.

Overcharge: The overcharge test evaluates battery safety when its voltage is taken above its maximum voltage limit. Cells that do not have explicit overcharge protection circuitry designed into them and that are to be used as part of a larger battery pack that affords such protection are exempt from this test. This test is performed by using a charging current that is 2 times the manufacturer's recommended charging current. The overcharge voltage level is dependent on the maximum voltage limit of the cell or battery. If the test is for a single cell or a battery with a voltage less than 18 V, the overcharge voltage level is either 2 times the

maximum voltage or 22 V, whichever is less. If the battery's maximum voltage is greater than 22 V, the overcharge voltage level is 1.2 times the maximum voltage. The overcharge condition is held for 24 h, and should not result in fire during or within 24 h of the test. For batteries that weigh less than 12 kg, the test must be repeated for 4 samples after their first cycle and 4 samples after 50 charge/discharge cycles. Specifications for the charge/discharge cycling procedure are not given in the manual. For batteries that weigh more than 12 kg, 2 samples must be tested after the first cycle and 2 samples must be tested after 25 charge/discharge cycles.

Forced discharge: The forced discharge test evaluates the ability of a cell or battery to withstand a forced discharge condition. This test is performed by connecting the cell or battery in series with a 12 V DC power supply with an internal current that matches the maximum discharge current recommended by the manufacturer. The test is defined by dividing the rated capacity by the test current applied. A fire should not occur during or within 7 days of the test. This test must be repeated for 10 fully charged samples and 10 fully discharged samples after their first cycle, and then each of the 10 samples should be tested again at a fully charged state and a fully discharged state after 50 charge/discharge cycles.

A summary of the tests and samples used is shown in Table 1.

Table 1 Summary of UN regulatory tests and required sample sizes

Test	Cells	Batteries
Altitude Simulation	10 fully charged cells 10 fully discharged cells	4 fully charged batteries 4 fully discharged batteries
Thermal		

Vibration	(Tests are performed sequentially on the same 20 samples)	(Tests are performed sequentially on the 8 samples)
Shock		
External Short Circuit		
Impact	5 cells	5 batteries
Overcharge	Cells that do not have overcharge protection circuitry are exempt from testing. Cells or batteries less than 12 kg: 4 samples after 1 charge/discharge cycle and 4 sample after 50 charge/discharge cycles Cells or batteries greater than 12 kg: 2 samples after 1 charge/discharge cycle and 2 samples after 25 charge/discharge cycles.	
Forced Discharge	10 fully charged cells after 1 charge/discharge cycle 10 fully discharged cells after 1 charge/discharge cycle 10 fully charged cells after 50 charge/discharge cycles 10 fully discharged cells after 50 charge/discharge cycles	10 fully charged batteries after 1 charge/discharge cycle 10 fully discharged batteries after 1 charge/discharge cycle 10 fully charged batteries after 50 charge/discharge cycles 10 fully discharged batteries after 50 charge/discharge cycles

Chapter 7: Hazards Associated with Degraded Batteries

The increased use of lithium-ion batteries in products such as electric and hybrid electric vehicles, E-bikes, and portable electronics results in vast quantities of used or degraded batteries. Wang et al. [36] estimated that 46 million kg of $LiCoO_2$ was used for fabricating 18,650 cells in 2006, all of which will eventually require disposal or recycling. Automotive manufacturers generally suggest battery replacement when the battery's capacity drops to 70%–80% of the original rated value. This leaves energy storage capabilities in degraded batteries with the possibility for second-use applications such as energy grid storage [37]. Other situations may arise where

degraded cells or batteries must be tested to validate warranty claims or processed for recycling. In all these cases, the shipment and transport of degraded cells or batteries will be required.

Currently, there are two special provisions outlined by the UN for shipping degraded batteries:

"Waste batteries and batteries being shipped for recycling or disposal are prohibited from air transport unless approved by the appropriate national authority of the State of Origin and the State of the Operator."
UN Special Provision A183

"Lithium batteries identified by the manufacturer as being defective for safety reasons, or that have been damaged, that have the potential of producing a dangerous evolution of heat, fire or short circuit are forbidden for transport (e.g. those being returned to the manufacturer for safety reasons)."
UN Special Provision A154

While a manufacturer may identify batteries as potentially defective, it is less clear whether a non-defective, degraded battery poses a safety risk. Saito et al. [38] found that degraded cells or batteries generate more self-heating at high rates of discharge due to the increase in internal resistance. Therefore, if a degraded battery experienced a short circuit, joule heating could pose a safety hazard. However, at the same time,

degraded cells or batteries are able to store less energy, meaning that a potential thermal event would release less energy and could be less catastrophic. Therefore, methods should be developed that evaluate if a previously used cell or battery is at a high risk of undergoing thermal runaway.

Certain use conditions predispose cells or batteries to undergo thermal runaway. Thermal runaway is perpetuated by an internal short circuit, which generates self-heating and causes the volatile electrolyte solvents to undergo exothermic reactions. If the temperature of the cell exceeds the melting point of the separator (e.g., 115 °C for polyolefin materials), further exothermic reactions can increase the cell's temperature, generate gases, and cause the battery to vent flammable electrolyte and gases [39]. Internal short circuits can be introduced into a cell in a number of ways, and all possible causes must be considered when determining if a degraded battery should also be considered a safety hazard.

Current Collector Corrosion and Dissolution

Shu et al. [40] observed corrosion of copper current collectors in electrolyte solvent solutions after 30 days of storage. This was attributed to trace amounts of water, which resulted in the formation of hydrofluoric acid within the cell. When a cell or battery is left in storage for an extended period, the copper current collector is susceptible to corrosion. Free copper particles within a cell or battery could eventually result in short-circuiting between the electrodes, especially if the cell or battery is put back into operation. Additionally, when the cell's voltage falls below 1.5 V, the copper current collector becomes unstable in the organic carbonate solvent

and can dissolve [41,42]. Any cell or battery that has been left in storage and has a terminal voltage below the minimum voltage specified by the manufacturer needs to be assessed for potential copper corrosion and dissolution prior to shipping.

Separator Shrinkage

The separator plays a key role in cell or battery safety as it prevents the anode and the cathode from short-circuiting. It is typically composed of single or multilayer polyolefin sheets, with the most common materials being polyethylene (PE) and polypropylene (PP). For polyolefin materials, thermally induced separator shrinkage occurs at approximately 110 °C, with the coverable area of the separator reducing by as much as 14% [43,44]. If the separator shrinks and exposes the edges of the electrodes, short-circuiting can occur and could result in a catastrophic failure. Batteries designed for higher-temperature applications may use a solid electrolyte such as Li_2S-P_2S_5 [45], in which case separator shrinkage is not an issue. The type of separator used in a degraded battery should be known before it is cleared for shipping. If a battery is known to have been stored at temperatures exceeding 90 °C, or if the storage/usage history of a battery is not known, then a representative sample should be disassembled and the separator inspected. Separators showing signs of shrinkage should be considered defective for safety reasons.

Contamination

Contamination due to poor quality control during the manufacturing process has been linked to battery overheating. In 2006, Sony recalled 4.1 million Dell laptop batteries due to contamination issues [46]. Metal particles found within the cells were causing

a puncture in the separator, leading to short-circuiting between the anode and the cathode. Metal contamination within a cell is often a result of spattering during current collector tab welding, but it can also be introduced due to poor environmental controls during assembly [47]. Moisture contamination is also a concern as it has been shown to result in the formation of hydrofluoric acid in lithium-ion cells containing $LiPF_6$ electrolytes [48]. Hydrofluoric acid can then etch cell materials, leading to rapid degradation or a short-circuit failure if stray metallic particles are dispersed throughout the cell.

One of the biggest challenges in battery reliability is the detection of trace contamination in assembled cells. Often, contamination issues are not highlighted until after failures have been observed. Any cell or battery that has an open recall for issues regarding contamination should be considered defective for safety reasons. When contamination particles result in internal short circuits, rapid self-discharge of the cell or battery is observed. Products that exhibit a self-discharge rate more than 1.5 times faster than what was described by the manufacturer should be considered defective for safety reasons.

Dendrite Growth

Lithium plating can occur on the surface of battery electrodes and cause internal short circuits [49]. The lithium plating side-reaction occurs when the potential difference between the electrode and electrolyte (over-potential) drops below zero, preventing the intended lithium intercalation reaction and resulting in a surface layer of metallic lithium. The over-potential can fall below zero when a cell or battery has been

charged at high current rates or at low temperatures [50]. When the surface of an electrode has undergone lithium plating, there is a risk of lithium dendrite formation. Lithium dendrites have the potential to puncture the separator and result in an internal short circuit and catastrophic failure. The formation of lithium dendrites can be partially reversed though a controlled discharge to facilitate re-intercalation [51]. However, detection of lithium plating is a challenge for BMSs, most of which use phenomenological-based models or equivalent circuit models to estimate the internal state of the cell or battery. Because most BMSs do not explicitly model the physical phenomena that occur in a cell or battery, lithium plating is typically not detected until there is a noticeable drop in performance or a thermal event. Any battery that has operated under high charge/discharge rates or in subzero working environments should be subjected to a 0.5C complete discharge to assure that no plated lithium exists on the electrode surfaces.

Chapter 8: Suggested Pre-shipping Tests

The safety regulatory tests outlined in Section 2 do not provide a reliable claim to safety if the cells have undergone some prior use in-between the time they were first tested and when they were shipped. Degradation effects may dampen or exacerbate safety risks depending on how the batteries were used. For example, batteries that operated in small stationary electronics would likely be more benign than ones used in unmanned aerial vehicles due to the nature of degradation associated with each type of usage condition.

To properly evaluate the air transport risks of second-use batteries, samples should undergo a rigorous but timely set of tests. These tests are designed specifically to identify and evaluate any safety risks in a population of cells.

Disassembly

In many cases, complete cell or battery usage histories are not available for determining the transport risks. However, a cell disassembly can be performed on selected samples known to have undergone the same field conditions as the remainder of the lot. Disassembly can be performed according to the guidelines outlined by Williard et al. [52]. The state of the disassembled cell can be assumed to represent the rest of the batteries under consideration if chosen correctly. In order to maximize safety, the cells exhibiting the greatest degradation (measured by capacity, internal resistance, and impedance) should be tested. Bulging of the cell's casing is often an indication of gas generation associated with degradation or abuse, therefore, bulging cells should also be selected. To obtain a conservative overview of a cell population, the cell with the most degradation by capacity, internal resistance, or impedance, and the cell displaying the most bulging (as indicated by the cell thickness) should be selected for disassembly.

When a cell is disassembled, the current collector should be inspected for signs of pitting corrosion and the separator should be inspected for shrinkage or puncture. The dimensions of the separator should be larger than the contact area between the anode and the cathode.

Issues involving possible contamination can be investigated using microscopy. The surface of the electrodes should be examined for evidence of foreign particles dispersed throughout the cell. All current collector tab connections should be investigated for the presence of weld splatter, and the full electrode should be scanned by optical microscopy to identify obvious metallic contamination. Lithium plating and dendrite growth may be harder to observe through optical microscopy and instead can be viewed with scanning electron microscopy (SEM). Zier et al. [49] developed a method to enhance observation of lithium plating by dyeing electrodes with OsO_4. This allowed a clearer observation of metallic lithium in a back-scattering image. If the battery has fallen below 2 V, the presence of free copper should also be investigated. While energy dispersive spectroscopy (EDS) can be used to identify metallic copper, additional methods are needed to properly quantify the amount of free copper in the battery.

Thermal and Mechanical Stress Testing

Incipient faults within a cell may not be easily detectable under low-stress conditions. However, applying thermal and mechanical loads to a battery can help to identify issues that are not otherwise apparent through typical voltage or resistance measurements. Situations may arise during usage wherein developing faults such as lithium dendrites, small tears in the separator, or disintegrated shards from current collectors greatly increase the risk of a short circuit but have not actually resulted in a bridge between the anode and the cathode. One way to identify if these situations are present within a battery is to apply thermal and mechanical loads to the battery at incremental levels until the battery has undergone failure. The magnitude of the

external load that results in the failure, as well as the nature of the failure itself, can be used to identify if the risk of a used battery has increased or decreased during its operational life. Degraded batteries under incremental loading can be benchmarked against the same type of batteries in an unused condition to determine if the temperature or amount of external pressure that causes failure has decreased. Additionally, if batteries in an unused state undergo failure without outgassing, or expelling of flaming electrolyte, then the used cells should undergo failure in a similar way. Catastrophic failures can be an indication that incipient faults have developed during usage. Two representative samples should be selected from a group of batteries to undergo temperature stress testing, and two samples should be selected to undergo mechanical testing. Additionally, four cells in an unused state should be procured from the manufacturer, and two unused cells should be subjected to the same temperature and mechanical tests as the used cells. The purpose of the unused cells is to set a benchmark for evaluating degradation.

Temperature stress testing should be performed in two different ways; the first method evaluates the properties of cell as a whole, while the second evaluates the safety properties of the materials themselves. In the first temperature stress test, eight cells should be selected from a group of batteries with similar usage histories. Measurements of DC resistance, open-circuit voltage, discharge capacity, and weight should be taken at the beginning of the test and after each incremental temperature exposure. The cells are then placed in a thermally controlled chamber, brought to 0 °C, and held at that temperature for 1 h. After 1 h of low-temperature exposure, cell

measurements are taken and the temperature is increased to 30 °C and held for 1 h. This process is repeated up to 150 °C or until the cell undergoes failure, which is defined in the same way as the safety regulatory tests outlined in Section 2. If failure occurs in the degraded cells more than 60 °C lower than observed in the unused cells, the degraded cells should be considered defective for safety reasons.

To evaluate the safety risks of the materials themselves, differential scanning calorimetry (DSC) can be performed individually on the anode and cathode materials. DSC can then be performed using the method described by Wen et al. [53]. DSC is performed by heating a sample and then measuring the temperature required to heat an electrode sample as compared to some reference material. This experiment can identify the specific temperatures at which thermally induced reactions occur in the electrode materials themselves. It also gives an indication of how much heat is released during an exothermic decomposition reaction. The results of DSC for degraded cells should be compared against the results of DSC for unused cells to evaluate if the activation temperatures for exothermic reactions within a cell have decreased as a result of usage.

To fully evaluate the safety of a cell, additional samples should be subjected to different pressure conditions. Pressure testing and cell characterization is described in Williard et al. [54] in which low-pressure testing is performed inside a sealed pressure chamber, and high pressure is simulated using a compressive load. The low-pressure testing is similar to the altitude test described by the UN standards, however, the test

begins at standard altitude and pressure, and drops at certain pressure intervals until a near-vacuum state is reached. During pressure testing, low-current-rate pulsed charge/discharge cycles are performed at each pressure level with a rest period in-between each pulse. This charge/discharge profile is identical to that required to perform galvanostatic intermittent titration technique (GITT) [55], which can allow for electrochemical safety characterization as described in the following section.

To evaluate high-pressure tests, compressive loading is applied to simulate hydrostatic loading. True hydrostatic loading can be achieved by testing a battery within a fluid at specified depths; however, capacity leakage may occur due to the conductivity of the fluid between the two terminals of a submerged battery. During compressive loading, low-current-rate pulsed charge/discharge cycles are performed in the same way as they are during low-pressure testing in order to electrochemically characterize the cell. Williard et al. [54] performed compressive loading using a dynamic materials analyzer in order to measure the amount of stress applied and the responding reaction force of the battery (which changes as the battery expands and contracts during charge/discharge).

Electrochemical Characterization

The tests outlined in the UN's *Manual of Tests and Criteria* [35] specify a number of electrical and mechanical tests that must be performed in order to certify that a cell or battery is safe for air transport. While these tests cover a broad range of possible scenarios, they do not address situations in which multiple stresses occur at the same time. For example, an external short-circuit test and a low-pressure test are specified,

but these tests are not performed together. During transport at high altitudes, if there is an external short circuit of a cell or battery, it is likely that it will occur in a low-pressure environment. It is unclear from these tests if a low-pressure environment would increase the risk of battery failure during a short-circuit event, vibration, or shock. Therefore, the true safety performance of a lithium-ion cell or battery during air transport is not completely tested.

One approach to address the concerns that multiple stress factors impact the safety of cells or batteries being transported by air would be to perform all the permutations of the eight tests together. However, this would require an infeasible number of tests to complete the certification of any particular cell or battery and would place an enormous burden on battery manufacturers and certification agencies. Rather than perform all of these tests, the relationship between thermal and mechanical loads on the electrochemical performance of batteries should be characterized and understood. Best practices can then be developed based on an understanding of the interactions between external stresses and the internal electrochemical phenomena that could lead to a thermal runaway or catastrophic failure.

To obtain information on how a cell or battery will behave under different loading scenarios, physical parameters should be measured to understand how they change in relation to each other under different stress conditions. One parameter of importance is a battery's diffusion coefficient. When performing compression or low-pressure testing on batteries, the voltage is typically monitored as a means to qualify a pass or

fail. However, the voltage in a battery under a mechanical load does not undergo a significant change unless a short circuit actually takes place. This prevents batteries from being evaluated with a high level of granularity and instead just produces a binary pass-or-fail result. By determining how the diffusion of a battery changes under different loading conditions and at different levels of usage, the health and relative safety can be much better quantified.

Wu and Chang [56] showed that the high rate of discharge properties of a battery is mainly limited by the diffusion of lithium ions inside a battery. Decreased lithium diffusion caused by temperature or pressure could result in a battery not being capable of delivering a high current discharge. If the cause of the high current discharge is an external short circuit and the diffusion of lithium is being hindered by some external pressure (or lack of external pressure in low altitudes), internal heating could occur faster than if the battery was at atmospheric pressure.

Testing by Williard et al. [54] has demonstrated changes in lithium diffusivity under different pressure conditions by means of GITT. From this study, it was found that increasing external pressure decreases lithium diffusion above 3.9 V. By increasing or decreasing external pressure to a magnitude that induces cell failure, and then relating lithium diffusion to the corresponding pressure, lithium diffusion can be used as a metric to determine a cell's risk for failure. This analysis can become critical in determining a cell's risk during air transport.

Chapter 9: Conclusion on Battery Transportation Regulations

The packaging and safeguards that are used for bulk shipments of lithium batteries on commercial planes pose hazards. The chain reaction initiated by internal short circuit, puncture, or other types of damage in a single lithium battery can be hazardous as the fire propagates from one package to the next. New ICAO proposals and guidelines for bulk shipments call for inserting gels or other types of cooling agents between batteries or power packs. If adopted, the changes would lead to higher costs and extra weight for shippers. The current safety tests cover a broad range of possible scenarios, however, these tests do not adequately address situations in which multiple simultaneous stresses act on the battery.

While reducing the SOC of batteries prior to shipping could help reduce the energy released during a battery thermal runaway event, it poses a few problems. If the batteries are shipped long distances under a wide range of ambient conditions, the batteries could self-discharge to an unsafe level. Additionally, the cells could experience performance degradation as a result of shipping and storage at low SOCs.

The development of stringent functional requirements for batteries in order to identify and mitigate all risks (even for batteries that have undergone previous use) is the most effective way of qualifying batteries to be shipped on-board air transport vessels. The battery literature contains a wealth of knowledge regarding the potential safety hazards of both new and used lithium-ion batteries; however, this knowledge has not been fully incorporated into safety standards. Additionally, new methodologies for assessing the safety of batteries are needed. It is not practical to disassemble a

representative sample of batteries prior to shipment. Rapid, nondestructive assessment of batteries and their risk of catastrophic failure are needed to economically ship batteries in a safe manner. This document considers the physical causes of failure in order to develop best practices for testing and evaluating battery transport safety.

Chapter 10: Electrochemical Models of Supercapacitors

Supercapacitors, also known as ultracapacitors and electric double layer capacitors (EDLCs), fill a niche in energy storage technology by providing a higher energy density than traditional electrostatic and electrolytic capacitors and higher power density than batteries and fuel cells. The first patent for the modern EDLC was granted in 1957 [57] and was marketed to support memory back-up devices in computers. Since that time, the range of potential applications for EDLCs is growing to include electric vehicles, uninterrupted power supplies, adjustable-speed drivers, photo voltaic cells [58], and hybrid battery/EDLC power sources [59,60].

In EDLCs, reduction of charge storage performance occurs over time and usage. Therefore, the design of a reliable power source must consider the operational life of EDLCs under expected usage conditions. Loss of capacitance and increase in resistance occurs when temperature and voltage stresses result in solvent co-intercalation, exfoliation of graphite electrodes, and the formation of surface films [61]. An increased operational voltage can accelerate degradation reactions, resulting in the oxidation of functional groups and the release of gaseous products such as CO2 and CO [62]. Above 3.7V, propylene carbonate in the electrolyte is oxidized, resulting in thick resistive film formation and excessive gas generation. Modeling the

relationship between operational voltage, temperature, and expected time to failure allows components to be qualified for specific operating conditions based on data gathered from accelerated life testing.

Several efforts have been made to model capacitor life under environmental and usage conditions. Hwang et al. [63] presented a Weibull-Arrhenius model to account for the statistical distribution of life at different operating temperatures. In this model, the scale parameter of the cumulative Weibull distribution function was substituted for the Arrhenius relationship, allowing statistical fitting results to be used to estimate the activation energy. EDLCs from eight manufacturers were analyzed [63], and activation energy values were found to range from 0.02 to 1.34. Gualous et al. [64] and Uno et al. [65] used a standard Arrhenius relationship to model the dependence of EDLC life on environmental temperature. The model was based on the assumption that lifetime is proportional to the inverse reaction rate of the degradation process.

Bohlen et al. [66] performed accelerated life testing using temperature and voltage to stress capacitor samples. Capacitor aging was quantified by the observed changes in the component values of an equivalent circuit model. The changes in the component values were then modeled with respect to time using a heuristic exponential relation. Parler [67] described a general life model for aluminum electrolytic capacitors that is composed of three factors, including base life, temperature, and voltage. Temperature dependence was described with the Arrhenius equation where Boltzmann's constant, the activation energy, and the base temperature were approximated in order to establish the "doubles every 10^{o}C rule" [64,68]. The

voltage multiplier has been modeled with a linear relationship or with a power law of the ratio between the actual and rated voltages $(V_r/V_a)^j$ where j is an exponent found to vary between 0 and 6. The power law relationship for voltage is the most accepted for aluminum electrolytic capacitors [67,69,70]. For EDLCs, charge separation occurs at the electrode interface; whereas aluminum electrolytic capacitors use a dialectic formed by a thin oxide film on the anode. The difference in operating principles and reliability between EDLCs and electrolytic capacitors can be reflected in the voltage multiplier. Excessive charging of an EDLC results in a leakage current across the electric double layer that, when charged under a constant current, causes the ΔV vs. Δt relation to deviate from its ideal linearity. The increased leakage current can be described by the Tafel equation in its exponential form [71] and is associated with a Faradaic decomposition of the electrolyte. Therefore, the voltage multiplier for EDLCs may be better described with an exponential relation.

Goltser et al. [72] proposed the Arrhenius-Eyring EDLC life model, which considers an exponential relationship for both the temperature and voltage factors. The model contains 3 constants, which are lumped parameters associated with the base life, activation energy, and voltage multiplier exponent. Accelerated life testing included nine different voltage and temperature stress conditions using a greater number of test samples at the lower stress conditions. Similar to Hwang [63], the failure distributions at each test condition were fit to the Weibull life distribution in order to determine the characteristic life.

Gualous et al. [64] and Bohlen et al. [66] used four test conditions (two temperatures and two voltages) and provided no evidence of the model prediction capability.

Additionally, Gualous [64] derived an equation to estimate the activation energy based on the extrapolation of 2 data points, while Bohlen [66] used the "double every 10^{o}C" rule to estimate the activation energy. Uno [65] determined the activation energy based on the slope of the Arrhenius plot. Goltser [72] did not specify a method of parameter optimization or explicitly relate the temperature constant to an activation energy. There have been no rigorous methods presented to determine the activation energy and voltage multiplier exponent that consider optimization based on a complete set of data.

This paper presents a model with a new voltage multiplier and compares it to the Arrhenius-Eyring EDLC life model and the aluminum electrolytic capacitor life model discussed in [66,69,70]. Additionally, a method is presented to determine the optimal parameters of the capacitor life models based on data coll1ected from accelerated life testing.

Chapter 11: Supercapacitor Testing Procedures

Twenty-nine commercial EDLCs (described by the manufacturer as ultracapacitors) were used in this study. Each sample had a rated capacitance of 100F and a rated voltage of 2.8V. The maximum charge/discharge current was specified as 74A, and the rated temperatures were between -40 and 60^{o}C. The manufacturer claimed an operating life of 10 years or 500,000 cycles at the rated voltage and a temperature of 25^{o}C. The failure criteria established by the manufacturer was a 30% decrease in capacitance or 100% increase in DC equivalent series resistance (ESR). Capacitance and resistance were measured periodically to monitor health and determine the time to failure of the capacitors. A constant current discharge at 2

Amps was performed to make the measurements. The current rate was chosen to be well below the maximum rated discharge current so that its effect on capacitor degradation could be considered negligible. Resistance was determined using the "intersection method" described in [64,65]. In this method, a line is extended backwards from the constant slope of the discharge voltage curve to the time at which the discharge began (denoted by t_1) to obtain the intersection voltage. The resistance is expressed in terms of the capacitance, C, the current, I, the first voltage recorded during discharge, U_1, the first voltage recorded during the constant slope discharge region U_2, and the times associated with the respective voltage measurements t_1 and t_2. The equation for resistance, R, is shown below in Figure 1. Capacitance was determined by computing the average of all instantaneous capacitance measurements spanning between 80% and 40% of the rated voltage. The instantaneous capacitance was calculated at each time step by dividing the change in time, dt, by the change in discharge voltage, dV(t), multiplied by the current, I(t), as shown in the equation in Figure 1.

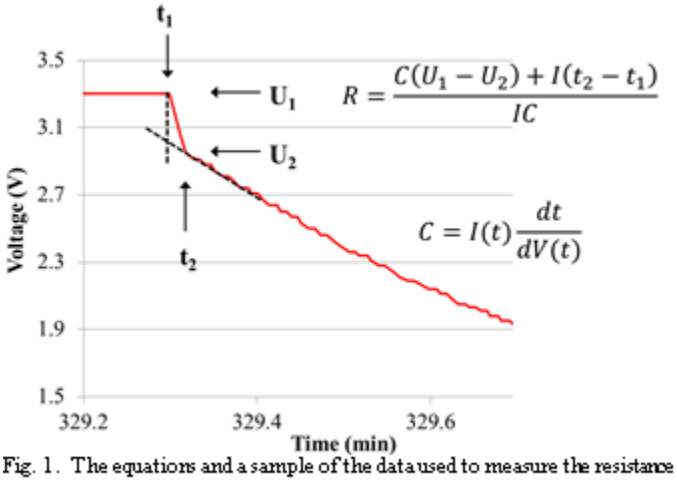

Fig. 1. The equations and a sample of the data used to measure the resistance and capacitance during each discharge.

The design of experiments involved two phases. The first phase was step stress testing, and the second phase was accelerated life testing, wherein the applied temperature and charging voltage were used to stress the capacitors. An often cited drawback of step stress testing is that failures that occur at high stress levels do not represent failures that occur at the lower stress levels found in use conditions [73]. For this study, step stress testing was not used to model life, but instead, was used to identify the maximum limit of temperature and voltage that the samples could withstand before an overstress failure occurred. Accelerated life testing was then conducted below this established maximum limit so that failures could be achieved in a reasonable time while also representing the failures that occur in use conditions. Figure 2 shows the general procedure for the two-phase life test. This test uses the results of step stress testing to determine the stress ceiling of the accelerated life test so that the temperatures and voltages used during accelerated life testing do not introduce abnormal failure modes that do not occur during actual usage conditions. While testing below the overstress condition, failures are generally linked to a common failure mechanism. By using a model to relate the stress level to the EDLC lifetime, tests at high stress levels (which can be completed quickly) can be used to predict the lifetime at lower stress levels, which would otherwise take years to test.

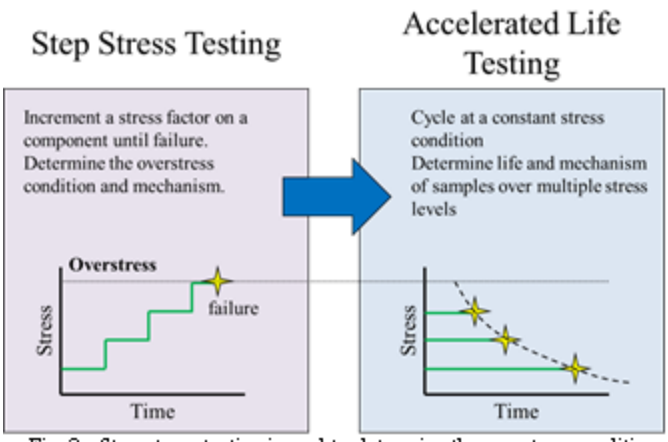

Fig. 2. Step stress testing is used to determine the overstress conditions, which gives the ceiling for stressing during accelerated life testing.

Five samples underwent step stress testing. Three samples were exposed to temperature step stress testing, and two samples underwent voltage step stress testing. For temperature step stress testing, the samples were first charged and discharged to obtain measurements for capacitance and resistance. Then, the samples were charged to their rated voltage, removed from the charger, and placed in a thermal chamber for 1 hour at a specified temperature. After storage in the thermal chamber, the capacitors were removed and allowed to cool before resistance and capacitance measurements were taken.

During voltage step stress testing, the capacitors were charged at a constant current of 1A and then held at a specified voltage for 1 hour in a constant voltage charging mode. After each hour of voltage stressing, the capacitor was discharged to collect resistance and capacitance measurements. The maximum current allowed during constant voltage charging was limited to 3A. When charging at voltages above 3.9V, it was found that the current could not converge to a trickle charge, resulting in joule heating and capacitor failure. The voltages and temperatures used during step stress testing are summarized in table 1.

TABLE I
STEP STRESS TESTING CONDITIONS

Sample	Voltage (V)	Temperature (°C)
1	2.8	25, 45, 65, 95, 125, 155
2	2.8	25, 45, 65, 95, 125, 155
3	2.8	25, 45, 65, 95, 125, 155
4	2.8, 3.0, 3.3, 3.6, 3.9, 4.2	Room Temperature
5	2.8, 3.1, 3.4, 3.7, 4.0	Room Temperature

Summary of the temperature and voltage conditions used during step stress testing.

Life testing was conducted by performing charge/discharge cycling inside a thermal chamber. The capacitor was charged at a constant current of 2A until the voltage reached a specific maximum voltage limit. The maximum voltage was held for 10 minutes and then a discharge at 2A was performed to collect capacitance and resistance measurements. Charge/discharge cycling continued until the capacitance decreased by 30% of its original value or the resistance increased by 100% of its original value. The specific temperature and voltage conditions for life testing were chosen based on the results of step stress testing. Therefore, these conditions are described in section 5.

The effect of temperature gradients throughout the thermal chamber was investigated because capacitor properties have found to be temperature dependent [74, 75, 76]. Life models often require the core temperature of the EDLC [67] to be provided as an input. To experimentally investigate thermal gradients, three thermocouples were placed inside the thermal chamber while heating to 110^{o}C at 18^{o}C/min. One of the

thermocouples was adhered to the top of a capacitor sample, one on the leads of the sample, and one was hanging free in the chamber to record the ambient temperature. The thermocouple measurements provide a conservative estimate of the difference between the capacitor core temperature and the chamber temperature. The thermocouple hanging free in the chamber showed that the temperature of the chamber is the first to reach 110^{o}C, while the temperatures at the leads and the top of the capacitor lag during convection heating of the sample. The maximum difference in temperature between the three thermocouples occur around four minutes after heating of the chamber begins and then converge to a steady state after 15 minutes of heating. To minimize the effects of thermal gradients on the resistance and capacitance measurements, cycling was started 5 minutes after the thermal chamber heating began. Because the constant voltage portion of the charging profile was maintained at the maximum voltage for ten minutes, there was sufficient time for the capacitor's core temperature to converge with the chamber temperature for the first capacitance and resistance measurement taken during discharge.

Chapter 12: Results of supercapacitor testing

The capacitance and resistance at each stress level during voltage step stress testing is shown for samples 4 and 5 in Figure 3. In sample 4, the final test condition at 4.2 V resulted in a hard failure of the capacitor, where the vent seal popped and the electrolyte leaked out, as shown in Figure 4. This hard failure occurred before the battery was able to be discharged, so no measurement was recorded during this step. A decrease in capacitance by more than 60% was noted at step stress levels of 4.0V and above. Between 2.8 and 3.9V, a 20% increase in resistance was observed, while

the capacitance remained unchanged. The sudden changes in capacitance and resistance show that the overstress failure mode brought on by oxidation of propylene carbonate in the electrolyte [6] was invoked at around 4.0V at room temperature.

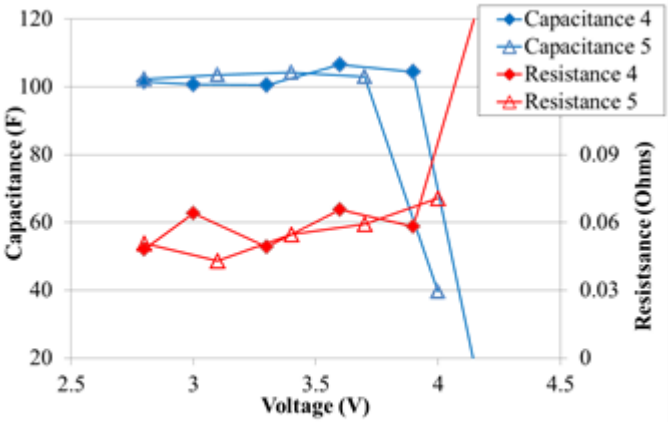

Fig. 3. The capacitance and resistance measured at each step of the voltage step stress test. The sudden change in properties at around 3.9V indicates that an abnormal failure mode was initiated at this voltage.

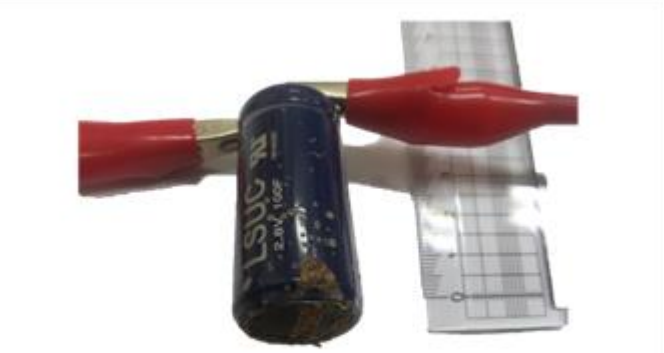

Fig. 4. Remains of expelled electrolyte seen on the casing of sample 4 after it failed during voltage step stress testing.

The results of the temperature step stress testing are shown in Figure 5. All the samples failed after storage at 155ºC. Significant bulging of the capacitors (likely due to gas evolution) became noticeable after storage at 95ºC for 1 hour. However, even with capacitor bulging, the resistance and capacitance values were still within the usable limits as defined by the manufacture's failure threshold. After failure at 155ºC, the vent seal in sample 2 was slightly ruptured and a 60% decrease in

capacitance increase was observed. In the other two samples, failure occurred due to a 100% increase in resistance criteria but not due to the loss of capacitance. Based on these results, 155°C was considered to be the temperature ceiling for further life testing.

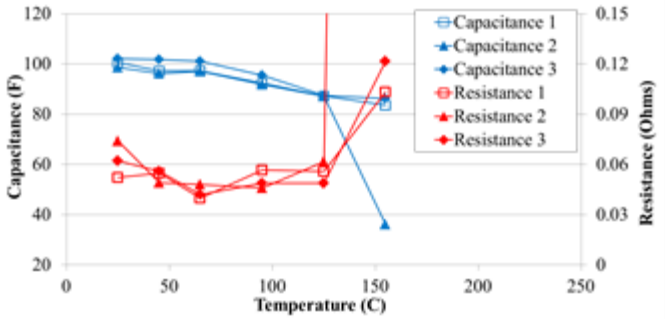

Fig. 5. Capacitance and resistance measured at each step of the temperature step stress test. The sudden change in properties between 125C and 150C indicate that an abnormal failure mode is initiated in this temperature region.

Step stress testing was used to determine the temperatures and voltages for accelerated life testing. Accelerated life testing was performed at 95°C, 110°C, and 125°C, which were approximately halfway between the maximum rated temperature (60°C) and the overstress temperature (155°C) to ensure that the test was sufficiently accelerated while remaining below the overstress conditions at which a new failure mode would be introduced.

Three different charging voltages were used at each temperature. Initially, a test was developed where the constant voltage stressing would be performed at 3.0, 3.3, and 3.6 V at each temperature. However, when attempting to charge a capacitor sample to 3.6V at 110°C, the voltage failed to reach the 3.6V condition during the constant current portion of the charging profile and after examination of the capacitor it was found to have experienced an overstress failure. The combined effect of temperate

and voltage on life was not known prior to testing, but it was evident that in order to prevent the overstress failure mode from occurring during life testing at high temperatures, the constant charge voltage should decrease as the ambient temperature increases. Therefore, the three charging voltages used for each temperature during accelerated life testing did not exceed 3.3V. The final conditions and the results from the life testing are summarized in Table 2.

The normalized capacitance degradation is shown in Figures 6-8, and the normalized resistance is shown in Figures 9-11. Similar behavior was observed between the capacitors tested under the same conditions, assuring that the unit to unit variations were small. The trend in capacitance degradation was generally monotonic with a few outlier data points, while the resistance data was noisy and in some cases decreased as the capacitors were tested (instead of increasing, as was expected). Failure occurred according to the 30% decrease in capacitance criteria, as opposed to the 100% increase in resistance for every capacitor tested during accelerated life testing.

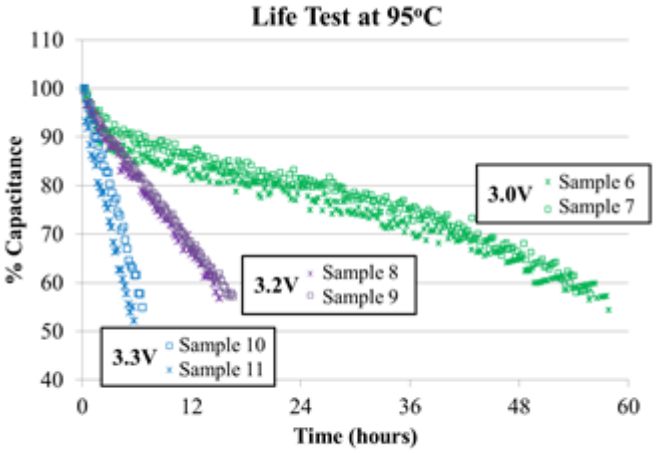

Fig. 6. Normalized capacitance during the accelerated life test for all samples tested at 95°C. The degradation rate is clearly accelerated with increased charging voltage.

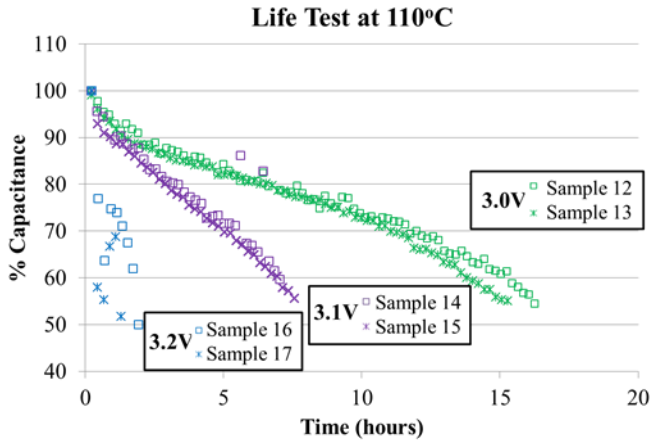

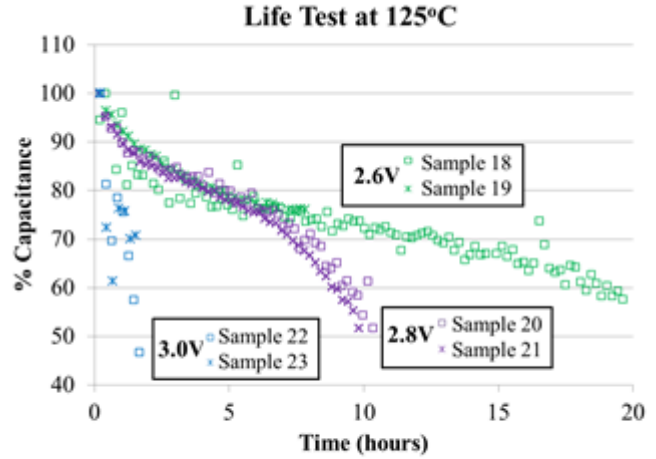

Fig. 8. Normalized capacitance during the accelerated life test for all samples tested at 125°C. The degradation trend at 2.6V and 2.8V were nearly identical up until the 6th hour of testing.

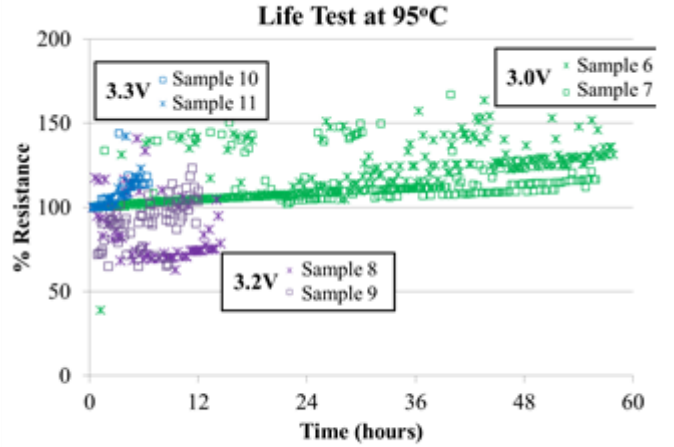

Fig. 9. Normalized resistance during the accelerated life test for all samples tested at 95°C. The trend in sample 8 decreases with increased usage.

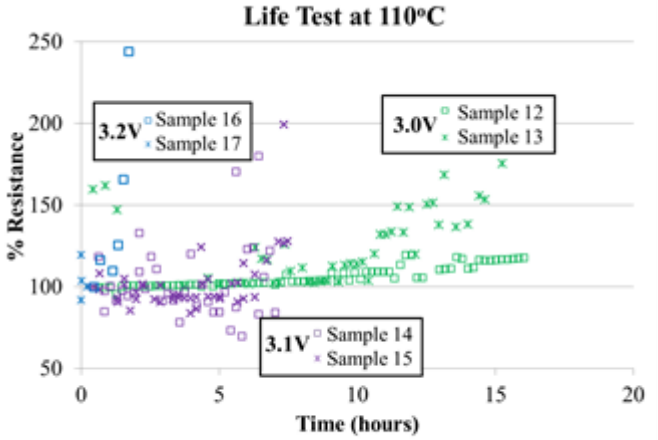

Fig. 10. Normalized resistance during the accelerated life test for all samples tested at 110°C.

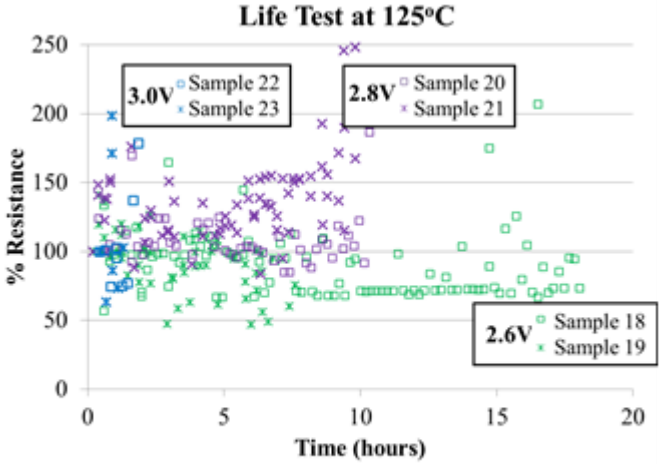

Fig. 11. Normalized resistance during the accelerated life test for all samples tested at 125°C. At this temperature there is significant noise in the measured resistance values.

Chapter 13: Supercapacitor Life Modeling

The life tests were conducted so that the failure of each sample occurred in less than 48 hours. This accelerated life testing can provide a significant time reduction for product qualification, provided that an acceleration factor can be determined to project capacitor lifetime to real-life usage conditions. To determine an acceleration factor, three models were developed and evaluated based on their ability to represent the generated life data given the temperature and maximum charging voltage. The first model was presented in previous studies [67,69], the second model introduces a new voltage multiplier which is the main contribution of this work, and the third model utilizes the Arrhenius- Eyring relationship.

The nonlinear temperature dependence associated with the rate of a chemical reaction is described by the Arrhenius equation. Because capacitor degradation is associated with electrochemical reactions that result in electrolyte degradation, an Arrhenius relationship is appropriate:

$$R(T_a) = Ae^{\frac{-E_a}{kT_a}} \quad (1)$$

where R is the reaction rate, A is an empirical coefficient, E_a is the activation energy in eV, k is the Boltzmann constant in eV K^{-1}, and T_a is the core temperature of the EDLC in Kelvin. By assuming that the life of a capacitor is directly related to the rate of degradation reactions, a life model can be generated by:

$$\frac{L_a}{L_r} = \frac{R(T_r)}{R(T_a)} = e^{\frac{E_a(T_r - T_a)}{kT_rT_a}} \quad (2)$$

where L_a is the expected operating life (time to failure), L_r is the rated life, and T_r is the rated temperature corresponding to the rated life. The rated values (denoted by the subscript r) serve as model constraints and are typically the rated life and

temperatures found in the manufacturer's data sheet. However, the rated values chosen by the engineer can be any data point that causes the model to adhere to a specific expected life under a given stress condition. Extensive life testing performed under a single temperature-voltage condition can be used to evaluate the peak of the life distribution. This can be used to provide rated values that will cause the model to give life predictions that are closer to the maximum likelihood of the life distribution. Using the rated conditions in the manufacturer's data sheet will generally result in conservative life predictions as manufactures claim a lower lifetime than what their products are capable of delivering in order to assure an acceptable reliability standard. To account for the effect of voltage on lifetime, a voltage multiplier M_v can be introduced to the life model:

$$L_a = M_v \left\{ L_r e^{\frac{E_a(T_r - T_a)}{kT_rT_a}} \right\} \quad (3)$$

As previously discussed, the most widely accepted voltage multiplier for aluminum electrolytic capacitors is given as a power law between the ratio of the rated voltage and the actual voltage [67,69,70], giving the final life model:

$$L_a(V_a, T_a) = \left(\frac{V_r}{V_a}\right)^j L_r e^{\frac{E_a(T_r - T_a)}{kT_rT_a}} \quad (4)$$

where *j* is the power of the voltage multiplier, V_a is the actual operational voltage and V_r is the rated voltage. Equation 4 will be denoted as Model 1 for the remainder of the paper. This model is compared with a new model (denoted as Model 2) that assumes a different form for the voltage multiplier. The new model also satisfies the following constraint:

For $V_a = V_r$ and $T_a = T_r \rightarrow L_r = L_a$

The voltage multiplier for Model 2 was motivated by the results of voltage step stress testing (Figure 3), which show that degradation occurs relatively slowly with increasing voltage until it reaches a point, at which degradation accelerates. This behavior cannot be expressed as a power law, which describes degradation as accelerating more rapidly at the beginning of voltage stressing and then flattening out as the voltage stressing continues to increase. To incorporate this behavior into the model, a negative exponential term was used as the voltage multiplier to yield the following equation for Model 2:

$$L_a(V_a, T_a) = \left[-e^{j(V_a - V_r)} + 2\right] L_r e^{\frac{E_a(T_r - T_a)}{kT_r T_a}} \quad (5)$$

The form of Model 2 is such that lifetime can be negative above certain values of voltage and temperature (depending on the model parameters). Therefore, the following condition was applied to Model 2 to assure that the lifetime values were never below zero:

$$if\ L_a(V_a, T_a) < 0\ then\ L_a(V_a, T_a) = 0$$

Model 3 as described by Goltser et al. [72] does not incorporate rated values or Boltzmann's constant into the equation and instead lumps all of these into three fitting parameters *A*, *B* and *D* which can be loosely related to the base life, temperature and voltage terms:

$$L_a(V_a, T_a) = Ae^{\frac{B}{T_a} + DV_a} \quad (6)$$

The general forms of Model 1, Model 2, and Model 3 are shown in Figure 12. This figure shows how only Model 2 is capable of capturing degradation behavior that accelerates with an increasing maximum operational voltage.

In order to determine the values of E_a and j, a constrained parameter least absolute deviations technique was applied. This method takes into account domain knowledge of the problem. It only considers realistic values of E_a and j to minimize the parameter search space. Previous attempts to characterize E_a [64] found that typical values range from 0.02 to 1.34 eV. The value of j is not as well characterized as E_a, but Parler [67]

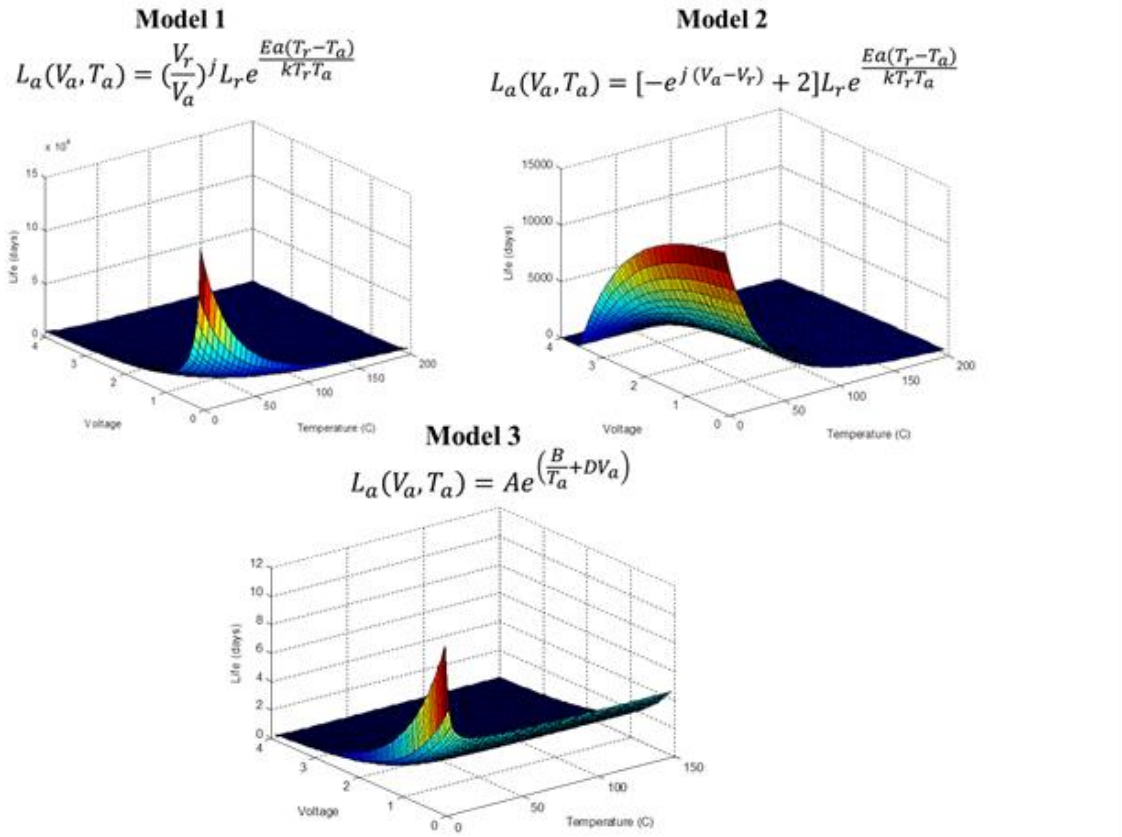

Fig. 12. General forms of Model 1, Model 2, and Model 3. Model 2 is unique in the sense that it asymptotes with decreasing voltage rather than increasing voltage as shown in Model 1 and Model 3.

claims that values range from 0 to 6. Therefore, in this work the search space for the independent model parameters was confined to:

$$j = \{x \in \mathbb{R}: 0 \leq x \leq 6\} \quad (6)$$

$$E_a = \{x \in \mathbb{R}: 0 \leq x \leq 2\} \quad (7)$$

Parameter values outside of this range result in unrealistic lifetimes exceeding 10^{13} days at temperatures above 0°C. Because the search space was confined to relatively limited values, a brute force search optimization technique could be used to minimize the absolute deviations objective function, which was formulated as:

$$S = \sum_{i=1}^{n} |y_i - L_a(V_{a_i}, T_{a_i})| \quad (8)$$

where y_i is the ith experimentally observed capacitor lifetime given at a charging voltage of V_{a_i} and a temperature of T_{a_i}. The values of y_i, V_{a_i}, and T_{a_i} correspond to the experimental lifetime, voltage and temperature values shown in Table 2.

To minimize the objective function, it is first expressed in terms of the parameter vectors β and Φ, which contain discrete values of j and Ea, respectively. The parameter vectors cover the search space described in equations (6) and (7). The size of the parameter vectors is denoted as p. The larger the value of p, the higher the resolution in the final parameter estimate. However, larger values of p also result in longer computation times.

$$\beta = \left[\frac{1*6}{p}, \frac{2*6}{p}, \ldots, \frac{i*6}{p}, \ldots, \frac{p*6}{p}\right] \quad (9)$$

$$\Phi = \left[\frac{1*2}{p}, \frac{2*2}{p}, \ldots, \frac{i*2}{p}, \ldots, \frac{p*2}{p}\right] \quad (10)$$

Substituting equations (4), (9) and (10) into equation (8) gives the following objective function for Model 1:

$$S(\beta, \Phi) = \sum_{i=1}^{n} \left| y_i - \left(\frac{V_r}{V_{a_i}}\right)^{\beta} L_r e^{\frac{\Phi(T_r - T_{a_i})}{kT_r T_{a_i}}} \right| \quad (11)$$

and substituting equations (5), (9) and (10) into equation (8) gives the following for Model 2:

$$S(\beta, \Phi) = \sum_{i=1}^{n} \left| y_i - \left[-e^{\beta\left(V_{a_i} - V_r\right)} + 2\right] L_r e^{\frac{\Phi(T_r - T_{a_i})}{kT_r T_{a_i}}} \right| \quad (12)$$

Solving these objective functions for all combinations of Φ and β yields a $p \times p$ matrix *S* for each model. The parameter values corresponding to the minimum element of *S* can then be taken as the optimized parameter values.

To optimize Model 3, the least absolute deviations method was extended to solve for the three unknown parameters. In this case there was no previous literature available to determine the parameter search space so a wider range was covered:

$$\begin{cases} A \\ B \\ D \end{cases} = \{x \in \mathbb{R}: -20 \leq x \leq 20\} \quad (13)$$

The parameter vectors β Φ and Θ were constructed to contain evenly distributed possible values of A, B, and D between the intervals of -20 and 20 with the interval distance governed by the size of the vector denoted by *p*. The final objective function for Model 3 was:

$$S(\beta, \Phi, \theta) = \sum_{i=1}^{n} \left| y_i - \theta e^{\frac{\Phi}{T} + \beta V} \right| \quad (14)$$

To compare the three models, the smallest elements of *S* from Model 1, Model 2 and Model 3 were found. The model that was able to produce the smallest absolute residuals between the predicted life and the generated test data was taken as the best model.

All of the models were used to fit the test data shown in Table 2. The models were evaluated between 0 and 4 volts and between 0 and 150°C. The least absolute deviations algorithm was written and executed in MATLAB, where p was set to 500 for Model 1 and Model 2, resulting in an S matrix containing 250,000 elements. This value of p provided a resolution to the hundredths place for the value of j and Ea. In the case of model 3, p was set to 200 due to the computation time required to optimize in an additional dimension. The resulting S array contained 8,000,000

elements but the resolution of parameters D, B and A was only achieved to the ten's place due to the higher dimentional search space. To achieve higher resolution, the optimization was performed iteratively where the search space was narrowed around the previously optimized parameter values.

Chapter 14: Discussion of Supercapacitor results

The optimization results for the three models are shown in Table 4. The mean absolute error is given as a metric to quantify the model performance. Based on the collected data, Model 2 had an absolute error that was more than 3 times smaller than Model 1 and Model 3. In Model 1 and Model 2 the activation energy (Ea) was determined to be 0.98 eV, which falls within the range of activation energy values described for super capacitors in the literature [63,64]. For the value of j, Model 1 did not converge within the bounds of the specified search space. Therefore, $j = 6$ (the highest value of j considered) was returned, implying that the true value of j to satisfy Model 1 was greater than 6. For Model 2, the value of j converged to 1.52. For Model 3, the parameters A, B, and D were found to be 5.87, 19.79, and -1.09, respectively.

Model 2's enhanced ability to fit the data generated in this testing is due to its inherent form. The negative exponential in the voltage multiplier results in an exponential drop in life with increased voltage similar to what is suggested by the Tafel equation with increased leakage current. This differs from both Model 1 and Model 3, which predict a deceleration of life with increasing voltage and an exponential increase in life at low temperatures and voltages. Further evidence of

Model 2's form can be seen in the results generated by Brouji et al [77] in which accelerated capacitance degradation is noted with an increased charge voltage.

TABLE II
ACCELERATED LIFE TESTING CONDITIONS

Sample	Voltage	Temperature	Life
6	3.0	95	40.7
7	3.0	95	43.5
8	3.2	95	10.8
9	3.2	95	10.9
10	3.3	95	4.5
11	3.3	95	3.2
12	3.0	110	11.6
13	3.0	110	10.8
14	3.1	110	6.4
15	3.1	110	4.8
16	3.2	110	1.3

TABLE III
OPTIMIZATION RESULTS

	Model 1	Model 2	Model 3
Mean absolute Error	6.39 Hr	1.90 Hr	6.65 Hr
E_a	0.98 eV	0.98 eV	-

A visualization of the surface described by equation (12) is shown in Figure 13 which confirms that the optimized values found by the constrained parameter least absolute deviations method returned a global minimum with a unique solution. It can be seen that with an increasing Ea along the Φ axis and increasing j along the β axis, the values of S display asymptotic behavior, thus assuring that there is no minimum

outside the bounds of the parameter search space. It is also interesting to note that under-estimation of the activation energy and j parameters result in large errors between the model and the data, whereas over estimating these parameters have a low sensitivity to the model error. Regardless of how much the parameters are overestimated the sum of errors between the model and the test data does not increase above 8 days. The resulting life model is shown in Figure 14, with the life-axis given on the log scale. In Figure 15, the life model is shown as a mesh plot in the region where the accelerated life testing was performed. The data points obtained from testing are shown in red. This figure shows that the model captures the trend observed during testing.

Further life testing was performed to evaluate the ability of the models to predict failure at temperatures and voltages lower than those used to train the model parameters. Six additional capacitors (denoted as A1-A6) were tested according to the

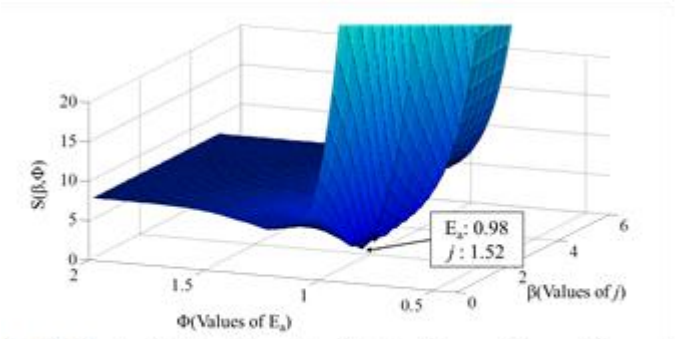

Fig. 13. The visualization of the surface that gives the sum of errors with respect to the input parameter values Ea and j for Model 2. The minimum value shown by the arrow is clearly a global minimum.

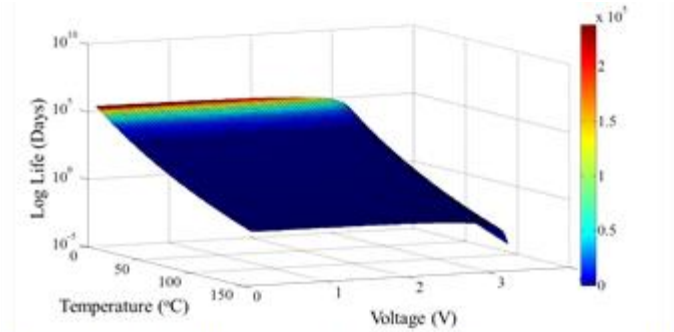

Fig. 14. The resulting life with respect to temperature and voltage predicted by Model 2 after optimization.

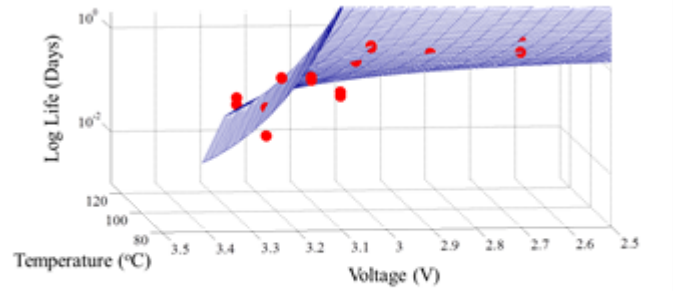

Fig. 15. The resulting life with respect to temperature and voltage predicted by Model 2 zoomed in on the region where accelerated life testing was performed. The data points determined from accelerated life testing are shown by the red circles.

profile used in accelerated life testing. In these tests, the capacitors were charged to a maximum voltage of 3.1V. Three of the additional capacitor samples were tested in an environment such that their core temperature was 77°C, and the other three were tested at 87°C. Under these conditions, Model 1 predicted a time to failure of 4.47 days and 1.67 days for 77°C and 87°C respectively at 3.1V. Model 2 predicted a time to failure of 5.34 days and 2.17 days for 77°C and 87°C respectively at 3.1V and Model 3 predicted a life time of 0.26 days and 0.25 days for 77°C and 87°C respectively. The mean absolute error between Model 1 and the resulting lifetimes of the additional capacitor samples was 1.355 days, while the mean absolute error for Model 2 was 0.670 days. Thus, Model 2 had a 50.5% lower prediction error than

Model 1. Model 3 showed poor performance when extrapolating beyond the data points used for testing. This is mainly due to its lack of rated values which are meant to constrain the model to a reasonable point in an unknown test space to improve extrapolation results. Figure 16 shows the output of Model 1 Model 2 and Model 3 at 3.1 volts, along with the results of samples 14 and 15 (which were each tested at a maximum voltage of 3.1V) and the

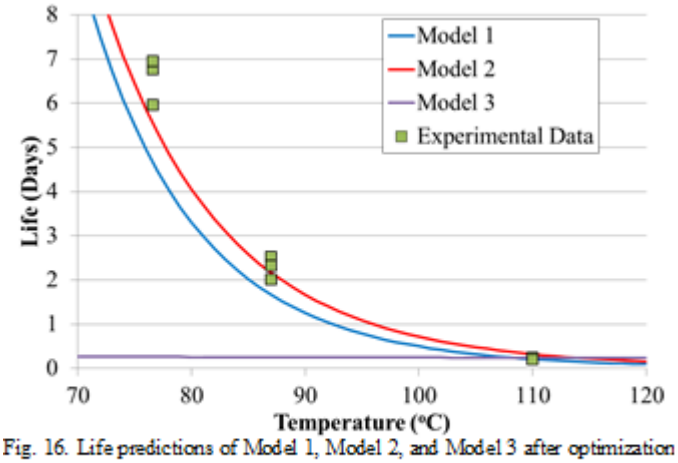

Fig. 16. Life predictions of Model 1, Model 2, and Model 3 after optimization at a maximum charge voltage of 3.1V. The data points at 88oC and 77oC test the model's extrapolation capabilities. Model 3 performed poorly as it was not constrained by rated conditions.

additional samples A1-A6.

Original equipment manufacturers (OEMs) must be able to estimate the time to failure of super-capacitors to ensure that they meet the reliability requirements of a particular design. Data sheets supplied by manufacturers may provide generic lifetime information, such as rated life, but the actual lifetime of a component is a function of its environmental and operating conditions. Therefore, the challenge for an OEM is to determine the actual lifetime of a component in field conditions within a short amount of time and with a limited number of test samples.

In order for life models to be useful to OEMs, they must be confident that the model predictions will accurately describe capacitors in working conditions. One of the

ways in which Model 1 and Model 2 manage the accuracy of extrapolation into an untested measurement space is through the establishment of the rated life, temperature, and voltage constraints. This feature allows models to incorporate information provided by previous testing or by the manufacturer's data sheet to limit the model's divergence up to the rated life criteria. If the life distribution of the rated life data is given by the manufacturer, further claims can be made to quantify the accuracy of the model's extrapolated predictions. Model 3, was not constrained by any rated life condition and showed poor model extrapolation capabilities after optimization. This was due to the fact that the model was only bounded by its ability to fit the high temperature and high voltage data without incorporating any a priori knowledge of what the capacitor life under low stress conditions might be. Additionally, assuring that the failure modes that occur during working conditions are the same as those that occur during accelerated testing theoretically supports the method of extrapolating a failure model into untested space.

The experimental work in this study was conducted at higher temperature and voltage stresses than what has been suggested by previous studies. Therefore, it is important to consider the failure mode that was invoked in these conditions and if this failure mode is indicative of failure at lower stresses. Activation energy can be used to infer classes of failure modes. Activation energies are associated with unique reactions, so when an alternative failure mode is introduced by a different dominating degradation reaction at a higher stress condition, the activation energy is expected to change [78]. The activation energy measured in this study fell within the range of activation energies calculated for 8 different EDLC manufacturers in Hwang's [63] study, and

was in fact within 0.03eV of one specific EDLC tested. Hwang [63] tested his samples at temperatures as low as 50^{o}C with lifetimes exceeding 1000 hours. The common activation energies observed between Hwang's [63] work and the present study suggest a common failure mode along this range of test conditions. While there is some evidence suggesting a common failure mechanism between the failures in this work and those conducted at lower stress conditions in Hwang's [63] work, care should be taken before extrapolating this model into lower test conditions. It is possible that another failure mode exists that becomes more dominant at lower stress conditions and can result in a deviation of life away from the modeled behavior. In this case, Model 1 or Model 3 may provide a better fit to the capacitor data. A complete capacitor model over a large range of stress conditions may be achieved with a spline that attaches multiple models based on the relevant failure modes.

In this work, 18 samples were tested for a total of 191 test hours (8 days). Three temperature conditions were used, and the longest that any one sample survived was 44 hours. Therefore, with three temperature chambers and a channel to charge and discharge each capacitor sample independently, these tests could be performed in less than 2 days. The voltage level was left as a flexible quantity that could be adjusted by the experimenter to ensure that accelerated testing does not result in an overstress failure. The result of the developed testing and optimization procedure yielded a life model for super capacitors that obtained the best fit to the generated test data while simultaneously adhering to the manufacturer's rated life claim. With this method, OEMs can input their expected usage conditions and obtain an estimate for the true operational life of a super capacitor.

Further applications of this method can be realized as part of a health monitoring system for energy storage devices. As developed in [79], this method could be incorporated into a system containing an on-board processor, memory storage, and sensing devices to provide real-time health information during capacitor operation. Capacitance, temperature, and voltage could be collected in real-time and used to update the model parameters during capacitor operation. This would be achieved by using trending analysis on the capacitance degradation curves, similar to what has been described for lithium-ion batteries [80]. By extrapolating the capacitance degradation curves, the failure times of the capacitors can be estimated during operation. These estimated failure times can be used to re-optimize the proposed failure model so that the parameters better represent the capacitors that are in operation. This would enhance the ability to predict failure as the capacitors operate.

Chapter 15: Supercapacitor Conclusions

A life model for electric double layer capacitors was developed by introducing a new voltage multiplier to describe the EDLC time to failure relationship with operational voltage. This voltage multiplier modifies the model form such that it captures the accelerated degradation that occurs at higher operational voltages. Compared to the Arrhenius- Eyring life model and the commonly accepted EDLC life model, which uses a power law for the voltage multiplier, the developed life model reduced the mean squared error between the model predictions and experimental data by more than three times and demonstrated better prediction accuracy when extrapolating the model to lower temperature and voltage conditions. Additionally, a method for optimizing capacitor life models in order to obtain the activation energy (Ea) and the

voltage multiplier coefficient (j) was developed. The method uses an optimization technique based on constrained parameter least absolute deviations to incorporate all of the collected test data to determine the model coefficients.

With the continued use of supercapacitor technology, there is a need to evaluate capacitor life to ensure that targeted reliability requirements are satisfied. The method presented in this work describes the suite of tests and data processing procedures that enables the calibration of an enhanced life model in less than 2 days of total testing, as compared to the several months required in previous methods. These results provide evidence that with an enhanced life model accelerated testing of super capacitors can be performed at higher stress conditions than what was previously considered.

Bibliography

1. T. Ohzuku, N. Matoba, Sawi, *J. Power Sources* 2001, 97, 73.
2. T. Ohzuku, Y. Iwakoshi, K. Sawai, *J. Electrochem. Soc.* 1993, 140, 2490.
3. D. J. Hankinson, J. Almlof, *J. Mol. Struc.-Theochem*. 1996, 388. 245.
4. J. L. Zang, Y. P. Zhao , *Int. J. Eng. Sci*. 2012, 61,156.
5. Z. Cui, F. Gao, J. Qu, *J. Mech. Phys. Solids* 2012, 60, 1280.
6. J. Christensen, J. Newman, *J. Electrochem. Soc*. 2006, 153, A1019.
7. R. Purkayastha, R. McMeeking, *Comp. Mater. Sci*. 2013. 80, 2.
8. X. Zhang, W. Shyy, A. Sastry, *J. Electrochem. Soc*. 2007. 154, A910.
9. S. Huang, F. Fan, J. Li, S. Zhang, T. Zhu, *Acta Mater.* 2013, 61, 4354.
10. W. Wu, X. Xiao, X. Huang, S. Yan, *Comp. Mater. Sci*. 2014, 83, 127.
11. M. Balhoff, K. Thompson, M. Hjortso, *Comput. Geosci.* 2007, 33, 393.
12. S. Golmon, K. Maute, M. Dunn, *Comput. Structures*. 2009, 87, 1567.
13. K. Lee, K. Smith, A. Pesaran, G. Kim, *J. Power Sources* 2013, 241, 20.
14. E. Jacques, M. H. Kjell, D. Zenkert, G. Lindbergh, *Electrochem. Commun.* 2013, 35, 65.
15. K. Hirai, T. Ichitsubo, T. Uda, A. Miyazaki, S. Yagi, E. Matsubara, *Acta. Mater.* 2008, 56, 1539.
16. T. Ichitsubo, S. Yukitani, K. Hirai, S. Yagi, T. Uda, E. Matsubara, *J. Mater. Chem.* 2011, 21, 2701.

17. E. Jacques, G. Lindbergh, D. Zenkerg, S. Leijonmarck, M. H. Kjell, *ACS Appl. Mater. Interfaces* 2015, 7, 13898.

18. R. Clarke, N. Wada, S. Solin, *Phys. Rev. Lett*. 1980, 44, 1616

19. H. Miyazaki, Y. Kuramoto, C. Horie, *J. Phys. Soc. Jpn.* 1984, 53, 1380.

20. R. Merkle, J. Maier, K.-D. Becker, M. Kreye, *Phys. Chem. Chem. Phys.* 2004, 6, 3633.

21. E. Bohn, T. Eckl, M. Kamlah, R. McMeeking, *J. Electrochem. Soc*. 2013, 160, 1638.

22. R. Fu, M. Xiao, S.-Y. Choe, *J. Power Sources*. 2013, 224, 211.

23. C. J. Wen, B. A. Boukamp, R. A. Huggins, *J. Electrochem. Soc.*1979, *126*, 2258.

24. Y. Zhu, C. Wang, *J. Phys. Chem. C* 2010, 114, 2830.

25. A. M. Dimiev, G. Ceriotti, N. Behabtu, D. Zakhidov, M. Pasquali, R. Saito, J. M. Tour, *ACS Nano* 2013, 7, 2773.

26. S. Al Hallaj, R. Venkatachalapathy, J. Prakash, J.R. Selman, *Journal of the Electrochemical Society*, 2000, 147, 2432

27. A. Funabiki, M. Inaba, T. Abe, Z. Ogumi, *J. Electrochem. Soc*. 1999, 146, 2443.

28. V. Sethuraman, L. Hardwick, V. Srinivasan, R. Kostecki, *J. Power Sources* 2010, 195, 3655.

29. W. H. Kruskal, W. A. Wallis, *J. Am. Stat. Assoc*. 1952, 47, 583.

30. A. Einstein, *Ann. Phys*. 1905, 322, 549.

31. W. Vautz, B. Bodeker, J. Baumbach, S. Bader, M. Westhoff, T. Perl, *Int. J. Ion Mobil. Spec*. 2009, 12, 47.

32. United Arab Emirates General Civil Aviation Authority, "UPS Boeing 747 cargo fire accident: Uncontained cargo fire leading to loss of control inflight and uncontrolled descent into terrain" AAIS Case Reference 13/2010 Available online at: http://www.gcaa.gov.ae/en/ePublication/admin/iradmin/Lists/Incidents%20Investigation%20Reports/Attachments/40/2010-2010%20-%20Final%20Report%20-%20Boeing%20747-44AF%20-%20N571UP%20-%20Report%2013%202010.pdf (accessed on 28 March 2016)

33. International Civil Aviation Organization (ICAO), *Technical Instructions for the Safe Transport of Dangerous Goods by Air*, Doc 9284, 2015.

34. International Air Transport Association (IATA), *Dangerous Goods Regulations*, 2015.

35. United Nations Economic Commission for Europe (UNECE), *Recommendations on the Transport of Dangerous Goods*: *Manual of Tests and Criteria*, 5th rev. ed. (2008).

36. Wang, Y.; Apelian, D.; Mishra, B.; Blanpain, B. Lithium ion battery recycling: A CR3 communication *J. Miner. Met. Mater. Soc*. **2011**, *Volume 63*, 10

37. Viswanathan, V.; Kintner-Meyer, M. Second use of transportation batteries: Maximizing the value of batteries for transportation and grid services. *IEEE Trans. Vehicular Technol.* **2011**, *Volume 60*

38. Saito, Y.; Shikano, M.; Kobayashi, H. Heat generation behavior during charging and discharging of lithium-ion batteries after long-time storage. *J. Power Sources* **2013**, *Volume 244*, 294–299

39. Jhu, C.-Y.; Wang, Y.-W.; Shu, C.-M.; Chuang, J.-C.; Wu, H.-C. Thermal explosion hazards of 18650 lithium ion batteries with a VSP2 adiabatic calorimeter. *J. Hazard. Mater.* **2011**, *Volume 192*, 99–107

40. Shu, J.; Shui, M.; Huang, F.; Xu, D.; Ren, Y.; Hou, L.; Cui, J.; Xu, J. Comparative study on surface behaviors of copper current collector in electrolyte for lithium-ion batteries *Electrochim. Acta* **2011**, *Volume 56*, 3006–3014

41. Maleki, H.; Howard, J. N. Effects of overdischarge on performance and thermal stability of a Li-ion cell. *J. Power Sources* **2006**, *Volume 160*, 1395–1402

42. Zhao, M.; Kariuki, S.; Dewald, H. D.; Lemke, F. R.; Staniewicz, J. R.; Plichta,, E. J.; Marsh, R. A. Electrochemical stability of copper in lithium-ion battery electrolytes. *J. Electrochem. Soc.* **2000**, *Volume 147*, 2874–2879

43. Orendorff C.J. The role of separators in lithium-ion cell safety. *Electrochem. Soc. Interface* **2012**, *Volume 21*, 61–65

44. Choi, J. A.; Kim, S. H.; Kim, D. W. Enhancement of thermal stability and cycling performance in lithium-ion cells through the use of ceramic-coated separators. *J. Power Sources* **2010**, *Volume 195*, 6192-6196

45. Kim, J.; Eom, M.; Noh, S.; Shin, D. Performance optimization of all-solid-state lithium ion batteries using Li_2S-P_2S_5 solid electrolyte and $LiCoO_2$ cathode. *Electron. Mater. Lett.* **2012**, *Volume 8*, 209–213

46. *PC World Australia* Available online at: http://www.pcworld.idg.com.au/article/163302/dell_sony_discussed_battery_problem_10_months_ago/ (accessed on 28 March 2016)

47. Cha, S.; Lithium secondary battery .U.S. Patent 20090317707 A1 2008

48. Lux, S. F.; Lucas, I. T.; Pollak, E.; Passerini, S.; Winter, M.; Kostecki, R. The mechanism of HF formation in $LiPF_6$ based organic carbonate electrolytes. *Electrochem. Commun.* **2012**, *Volume 14*, 47–50

49. Zier, M.; Scheiba, F.; Oswald, S.; Thomas, J.; Goers, D.; Scherer, T.; Klose, M.; Ehrenberg, H.; Eckert, J. Lithium dendrite and SEI investigation using OsO_4. *J. Power Sources* **2014**, *Volume 266* 198–207

50. Zhang, S. S.; Xu, K.; Jow, T. R. Study of the charging process of a $LiCoO_2$-based Li-ion battery. *J. Power Sources* **2006**, *Volume 160*, 1349–1354

51. Petzl, M.; Danzer, M. Nondestructive detection, characterization, and quantification of lithium plating in commercial lithium-ion batteries. *J. Power Sources* **2014**, *Volume 254*, 80–87

52. Williard, N.; Sood, B.; Osterman, M.; Pecht, M. Disassembly methodology for conducting failure analysis on lithium-ion batteries. *J. Mater. Sci.: Mater. Electron.* **2011**, *Volume 22*, 1616–1630

53. Wen, C.-Y.; Jhu, C.-Y.; Wang, Y.-W.; Chaing, C.-C.; Shu, C.-M. Thermal runaway features of 18650 lithium-ion batteries for $LiFePO_4$ cathode material by DSC and VSP2. *J. Thermal Anal. Calorim*. **2012**, *Volume* 109, 1297–1302

54. Williard, N.; Hendricks, C.; Chung, J. S.; Pecht, M. Effects of external pressure on lithium diffusion in lithium-ion batteries. Submitted for publication.

55. Wen, C.J.; Boukamp, B. A.; Huggins, R. A. Thermodynamic and mass transport properties of "LiAl". *J. Electrochem. Soc.* **1979**, *Volume 126*, 12

56. Wu, M.-S.; Chiang, P.-C. High-rate capability of lithium-ion batteries after storing at elevated temperature. *Electrochim. Acta*. **2007**, *Volume 52*, 3719–3725.

57. H.I. Becker "Low Voltage Electrolytic Capacitor," US Patent 2800616, July 23, 1957.

58. P. Sharma, T.S. Bhatti "A review on electrochemical double-layer capacitors," Energy Conversion and Management, vol. 51, pp. 2901-2912, 2010.

59. M.E. Galvin, W.G. Hurley, "Optimization of a photovoltaic battery ultracapacitor hybrid energy storage system," Solar Energy, vol. 86, pp. 3009-3020, 2012.

60. Kuperman, I. Aharon, "Battery-ultracapacitor hybrids for pulsed current loads: A review," Renewable and Sustainable Energy Reviews, vol. 15, pp. 981-992, 2011.

61. F. Campana, M. Hahn, A. Foelske, P. Ruch, R. Kotz, H. Siegenthaler, "Intercalation into and film formation on pyrolytic graphite in a

supercapacitor-type electrolyte (C2H5)4NBF4/ propylene carbonate" Electrochemistry Communications, vol.8, pp 1363-1368, 2006.

62. S. Ishimoto, Y. Asakawa, M. Shinya, K. Naoi "Degradation responses of Activated-Carbon-Based EDLCs for Higher Voltage Operation and Their Factors" Journal of the Electrochemical Society, vol. 156, pp. A563-A571, 2009
63. D-H Hwang, J-W Park, J-H Jung, "A study on the lifetime comparison for Electric Double Layer Capacitors using Accelerated Degradation Test" IEEE International Conf. on Quality, Reliability, Risk, Maintenance, and Safety Engineering, pp. 302-307 ISBN 978-1-4577-1229-6, 2011
64. H. Gualous, R. Gallay, G. Alcicek, B. Tala-Ighil, A. Oukaour, B. Boudart, Ph. Makany, "Supercapacitor ageing at constant temperature and constant voltage and thermal shock," Microelectronics Reliability, vol. 50, pp. 1783-1788, 2010.
65. M. Uno, K. Tanaka, "Accelerated Charge-Discharge Cycling Test and Cycle Life Prediction Model for Supercapacitors in Alternative Battery Applications" IEEE Transactions on Industrial Electronics, vol. 59, no. 12, December 2012
66. O. Bohlen, J. Kowal, D. Sauer "Ageing behavior of electrochemical double layer capacitors Part I. Experimental study and ageing model," Journal of Power Sources, vol. 172, pp. 468-475, 2007.
67. S. Parler "Deriving Life Multipliers for Electrolytic Capacitors," IEEE Power Electronics Society Newsletter, vol 16. No. 1, pp. 11-12, 2004.

68. T.C. Hofelich, M.S. LaBarge “On the use and misuse of detected onset temperature of calorimetric experiments for reactive chemicals,” Journal of Loss Prevention in the Process Industries, vol. 15 pp. 163-168, 2002.
69. Ma, Hao, and Linguo Wang. "Fault diagnosis and failure prediction of aluminum electrolytic capacitors in power electronic converters," Industrial Electronics Society, IECON 31st Annual Conference of IEEE. IEEE, 2005.
70. J.A. Lauber, "Aluminum electrolytic capacitors-Reliability, expected life and shelf capability," Sprague Technical Paper, TP83-9, 1985.10.
71. B.E.Conway, “Electrochemical Supercapacitors: Science Fundamentals and Technological Applications, first ed.,” New York: Kluwer Academic/ Plenum Publishers, 1999.
72. Goltser, I., S. Butler, and J. R. Miller. "Reliability assessment of electrochemical capacitors: method demonstration using 1-F commercial components." Proc. 15th international seminar on double layer capacitors, pp. 215, Deerfield Beach (USA). 2005.
73. W.B. Nelson “Accelerated Testing: Statistical Models, Test Plans, and Data Analysis” Hoboken, New Jersey: John Wiley & Sons, Inc. 2004
74. M. Taniguchi, D. Tashima, M. Otsubo, “Temperature Dependence of Capacitance in Electrochemical Super Capacitor,” Annual Report Conference on Electrical Insulation and Dielectric Phenomena. IEEE, 2007.
75. R. Kotz, M. Hahn, R. Gallay “Temperature behavior and impedance fundamentals of supercapacitors,” Journal of Power Sources, vol. 154, pp. 550-555, 2006.

76. J. Reszko-Zygmunt, S. Sokolowski, D. Henderson, D. Boda “Temperature dependence of the double layer capacitance for the restricted primitive model of an electrolyte solution from a density functional approach,” The Journal of Chemical Physics, vol. 122, 084504, 2005.
77. E.H.E Brouji, O. Briat, J-M Vinassa, N. Bertrand, E. Woirgard, “Impact of Calendarr Life and Cycling Ageing on Supercapacitor Performance,” IEEE Transactions on Vehicular Technology, vol. 58, no. 8, October 2009
78. M.L. Moeschberger “Life Test Under Dependent Competing Causes of Failure,” Technometrics, vol. 16, pp. 39-47, 1974.
79. N.M. Vichare, M.G. Pecht “Prognostics and Health Management of Electronics,” IEEE Transactions on Components and Packaging Technologies, Vol 29 No.1, pp 222-229, 2006.
80. W. He, N. Williard, M. Osterman, M. Pecht. “Prognostics of lithium-ion batteries based on Dempster-Shafer theory and the Bayesian Monte Carlo method,” Journal of Power Sources, vol. 196, pp. 10314-10321, 2011.